NASA/CR—2010-216779

Inlet Flow Control and Prediction Technologies for Embedded Propulsion Systems

Summary Report for Fiscal Year 2009

Michelle L. McMillan
SynGenics Corporation, St. Louis, Missouri

Abe Gissen and Bojan Vukasinovic
Georgia Institute of Technology, Atlanta, Georgia

Matthew T. Lakebrink
The Boeing Company, St. Louis, Missouri

Ari Glezer
Georgia Institute of Technology, Atlanta, Georgia

Mori Mani and James Mace
The Boeing Company, St. Louis, Missouri

October 2010

NASA STI Program . . . in Profile

Since its founding, NASA has been dedicated to the advancement of aeronautics and space science. The NASA Scientific and Technical Information (STI) program plays a key part in helping NASA maintain this important role.

The NASA STI Program operates under the auspices of the Agency Chief Information Officer. It collects, organizes, provides for archiving, and disseminates NASA's STI. The NASA STI program provides access to the NASA Aeronautics and Space Database and its public interface, the NASA Technical Reports Server, thus providing one of the largest collections of aeronautical and space science STI in the world. Results are published in both non-NASA channels and by NASA in the NASA STI Report Series, which includes the following report types:

- TECHNICAL PUBLICATION. Reports of completed research or a major significant phase of research that present the results of NASA programs and include extensive data or theoretical analysis. Includes compilations of significant scientific and technical data and information deemed to be of continuing reference value. NASA counterpart of peer-reviewed formal professional papers but has less stringent limitations on manuscript length and extent of graphic presentations.

- TECHNICAL MEMORANDUM. Scientific and technical findings that are preliminary or of specialized interest, e.g., quick release reports, working papers, and bibliographies that contain minimal annotation. Does not contain extensive analysis.

- CONTRACTOR REPORT. Scientific and technical findings by NASA-sponsored contractors and grantees.

- CONFERENCE PUBLICATION. Collected papers from scientific and technical conferences, symposia, seminars, or other meetings sponsored or cosponsored by NASA.

- SPECIAL PUBLICATION. Scientific, technical, or historical information from NASA programs, projects, and missions, often concerned with subjects having substantial public interest.

- TECHNICAL TRANSLATION. English-language translations of foreign scientific and technical material pertinent to NASA's mission.

Specialized services also include creating custom thesauri, building customized databases, organizing and publishing research results.

For more information about the NASA STI program, see the following:

- Access the NASA STI program home page at *http://www.sti.nasa.gov*

- E-mail your question via the Internet to *help@sti.nasa.gov*

- Fax your question to the NASA STI Help Desk at 443–757–5803

- Telephone the NASA STI Help Desk at 443–757–5802

- Write to:
  NASA Center for AeroSpace Information (CASI)
  7115 Standard Drive
  Hanover, MD 21076–1320

NASA/CR—2010-216779

Inlet Flow Control and Prediction Technologies for Embedded Propulsion Systems

Summary Report for Fiscal Year 2009

Michelle L. McMillan
SynGenics Corporation, St. Louis, Missouri

Abe Gissen and Bojan Vukasinovic
Georgia Institute of Technology, Atlanta, Georgia

Matthew T. Lakebrink
The Boeing Company, St. Louis, Missouri

Ari Glezer
Georgia Institute of Technology, Atlanta, Georgia

Mori Mani and James Mace
The Boeing Company, St. Louis, Missouri

Prepared under Contract NNC07CB76C

National Aeronautics and
Space Administration

Glenn Research Center
Cleveland, Ohio 44135

October 2010

Acknowledgments

This work was sponsored by the Fundamental Aeronautics Program at the NASA Glenn Research Center.

This report contains preliminary findings, subject to revision as analysis proceeds.

This work was sponsored by the Fundamental Aeronautics Program at the NASA Glenn Research Center.

Level of Review: This material has been technically reviewed by NASA technical management.

Available from

NASA Center for Aerospace Information
7115 Standard Drive
Hanover, MD 21076–1320

National Technical Information Service
5301 Shawnee Road
Alexandria, VA 22312

Available electronically at http://gltrs.grc.nasa.gov

Preface

This report documents the fundamental aeronautics research performed by The Boeing Company under NASA Contract No. NNC07CB76C during the Fiscal Year 2009. Subcontractors supporting The Boeing Company in this Contract were SynGenics Corporation and Georgia Institute of Technology. Ms. Julie Dudek of NASA served as the Contract Officer's Technical Representative.

Executive Summary

Fail-safe, hybrid flow control (HFC) may be an enabling technology for meeting high-speed cruise efficiency, low noise signature, and reduced fuel burn goals for future HWB aircraft with embedded engines. The objectives of the Boeing IFCPT program are to develop flow-control technologies for highly integrated, offset inlets, as well as, to develop and improve novel test methods and validated tools for predicting active HFC effectiveness in managing inlet pressure distortion. The approach to accomplish the objectives encompasses experimental investigations of flow-control devices conducted in combination with numerical simulations incorporating robust flow-control-device modeling and advanced Computational Fluid Dynamics (CFD) tools.

In support of the program objective to develop flow-control technologies, the interaction of surface-mounted, passive and active flow-control devices with a Mach 0.5 cross flow were examined in a small-scale wind tunnel. The evolution of streamwise vortices induced by the flow control was investigated in an adverse pressure gradient consistent with the pressure gradient within a diffuser compatible with future HWB vehicles. Counter-rotating-vortex pairs and single-sense vortices were formed and characterized using passive microramps and microvanes, respectively. Similar streamwise vortices were also generated using synthetic jet actuators. Finally, hybrid actuation approaches were demonstrated where a passive microvane and active synthetic jet were designed and operated in a tandem arrangement, such that the induced vorticity from the active device enhanced the control of the passive device, improving the overall control effectiveness.

In support of the program objective to improve and validate tools and test methods for predicting active, hybrid flow-control performance, simulations of isolated devices in the Georgia Institute of Technology FMRL tunnel test section with the profiled wall were conducted. Results of the numerical simulations were validated against experimental data. The sensitivity of numeric results to grid resolution, turbulence model, and viscous-flux-calculation technique was examined. A grid refinement study was conducted to establish the grid size required for grid-independent solutions. Multiple turbulence models were used in simulations, and results were validated against experimental data. Comparisons of numerical simulations against experimental data showed that the Spalart-Allmaras (SA) turbulence model most accurately captured the microvane-induced vorticity in an adverse pressure gradient in Mach 0.5 flow. In general, the simulations over-predicted vortex strength, especially the downwash component. However, the qualitative shape of the vortex and its general influence on the flowfield were captured well by simulation.

Also in support of the objective to improve test techniques, numerical simulations of a Boundary-Layer-Ingesting (BLI) offset inlet duct consistent with that in the HWB vehicle were conducted during the current reporting period. These simulations were used to support the development of the test technique for simulating BLI inlet flow in an isolated diffuser. Specifically, a boundary-layer profile at the duct entrance that produced AIP distortion levels and patterns consistent with BLI inlets was defined. This profile could be replicated experimentally with the use of a fence installed near the duct entrance.

Following the establishment of test and analysis techniques, microvane and microramp, passive, flow-control devices were simulated in the offset BLI inlet duct to assess the predicted performance benefits of these devices at the Aerodynamic Interface Plane (AIP). Benefits were quantified in terms of recovery and distortion reduction from the baseline, non-actuated flow. Microvane arrays were found to be significantly more effective than microramp arrays at improving recovery and distortion in BLI inlet ducts, as they produced the large-scale, vortical structures necessary to redistribute the ingested, low-energy boundary layer fluid at the AIP into more favorable engine-face patterns.

Finally, SA and Shear-Stress-Transport (SST) turbulence models were employed with a hybrid Reynolds-Averaged Navier-Stokes / Large Eddie Simulation (RANS/LES) model to improve prediction capabilities by developing the tools necessary to simulate the time-dependent flow features and attempt to predict dynamic distortion accurately in an offset, BLI inlet duct. This work will continue into the final year of this program. As experimental data is obtained for the duct test configurations, numerical

simulations will be validated against the data. Using this data, the prediction tool will be enhanced to improve dynamic distortion prediction capabilities in offset diffusers.

Future work on this effort includes detailed experimental measurements of active, passive, and hybrid flow control in a BLI inlet diffuser. Benefits of flow control will be quantified in terms of recovery, as well as, steady-state and dynamic distortion. Experimental data will be used to validate and tailor hybrid RANS/LES turbulence models for accurate, numerical prediction of dynamic distortion. Finally, system-level payoffs and penalties of flow-control in BLI ducts will be assessed in terms of TOGW, performance, and risk.

Contents

List of Figures

Introduction

This document reports on the progress accomplished during Fiscal Year 2009 for an element of the NASA AMRD Fundamental Aeronautics program effort, Appendix A.2, Topic A.2.4.2—Integrated Embedded Propulsion Systems. This work focuses on developing prediction tools for innovative aeronautical technologies for HWB aircraft configurations.

Background

Major technology extensions beyond current activities are needed to obtain high-speed cruise efficiency and low noise while reducing field lengths for HWB aircraft. The use of embedded turbofan engines in this wing / body aircraft, Figure 1, is being studied as a means to attain both high-speed cruise efficiency and low noise signature and fuel burn. Boeing is advancing both inlet technologies and prediction tools specifically focused at lowering and managing flow distortion using fail-safe, hybrid flow-control technologies. The investigations are to advance prediction methods for inlet flows by applying designed experiments using integrated Computational Fluid Dynamics (CFD) and tests to establish a database in a relevant environment and validate the methods.

This program supports the NASA Fundamental Aeronautics Program goal to pursue long-term, cutting-edge research in all flight regimes to produce data, knowledge, and design tools that are applicable across a broad range of vehicles by applying fail-safe hybrid flow-control technologies to manage flow distortion, thereby attaining both high-speed cruise efficiency and low noise signature. Furthermore, The Boeing Company is working in collaboration with the NASA Glenn Research Center (GRC), Georgia Institute of Technology, and SynGenics Corporation to extend the current state-of-the-art in active, hybrid flow control analytical design tools. Hybrid flow control analytical design tools are being validated through component-level testing, in an environment relative to embedded inlets of future-generation, HWB aircraft designs. This not only supports the aforementioned strategic goal, but leads directly to the strategic outcome of developing multidisciplinary design, analysis, and optimization capabilities.

Scope

The Boeing program, as depicted in Figure 2, combines technology advances made at the GRC in robust modeling of flow-control systems with advances in flow-control device modeling and testing at Boeing and Georgia Institute of Technology. The combination of testing and numerical simulation, integrated with the robust design methods from SynGenics, makes it possible to improve and validate current, state-of-the-art prediction tools necessary to quantify the benefits and optimize the design of flow-control systems in advanced inlets. To arrive at a demonstration of the hybrid system in a laboratory environment (TRL of 4) at the completion of the 3-year program, in collaboration with GRC, we will design experiments where data from test and CFD are used to produce response surfaces representing performance of inlet flow-control-system-design features. This technology base forms the foundation on which the hybrid system will be designed.

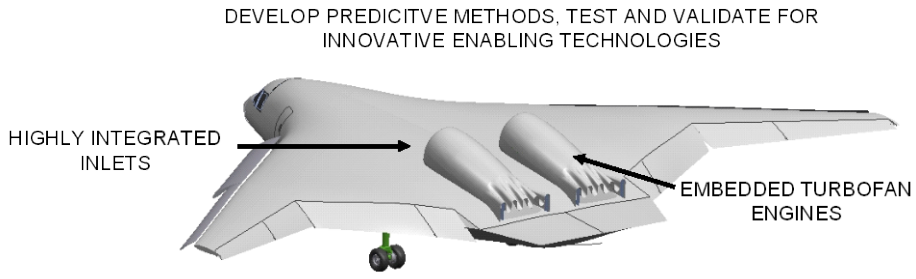

Figure 1.—“N+2” next generation HWB aircraft.

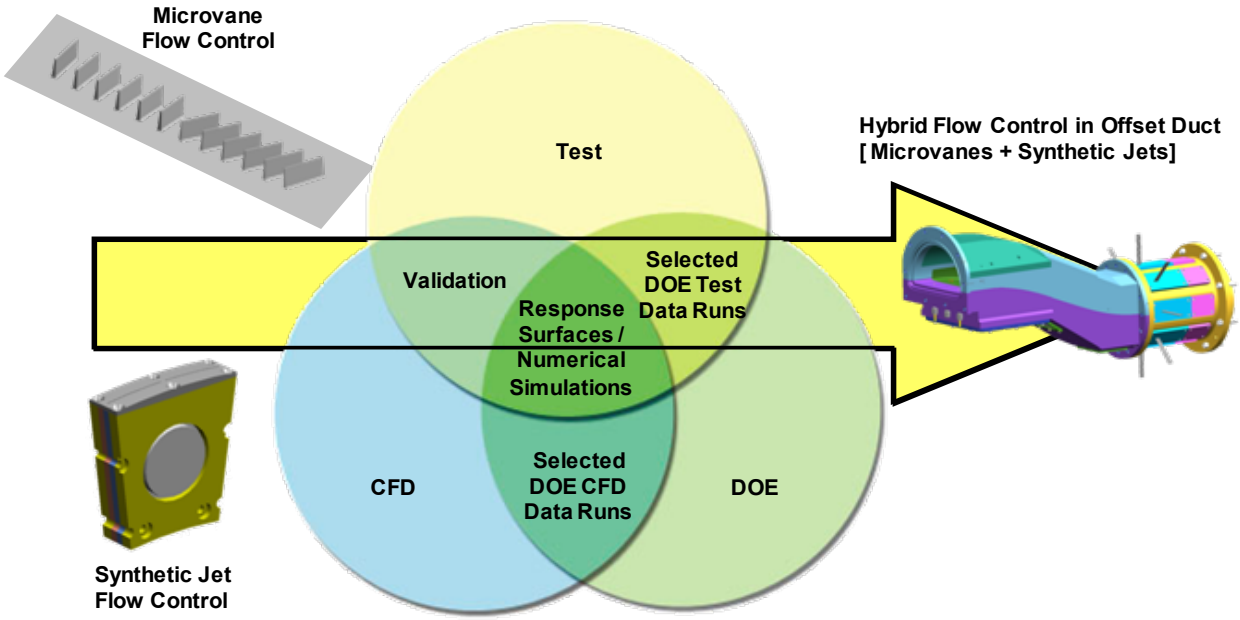

Figure 2.—Plan to improve and validate numerical analysis tools and develop advanced hybrid active flow control system for improved performance, reduced weight, and reduced emissions.

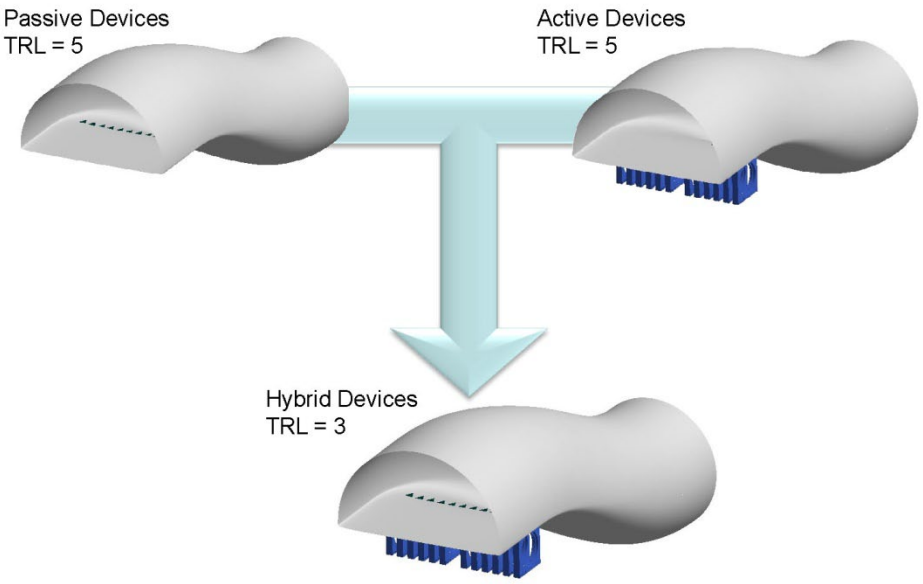

Figure 3.—Boeing's microvane/microjet hybrid flow control concept.

Boeing has been conducting research on an earlier variation of a hybrid flow-control system for an inlet. This earlier system combines passive microvanes and active microjets into an integrated hybrid system, Figure 3. The passive microvanes ensure flight-critical engine operability, while the active microjets provide flight-mission operability. With this earlier hybrid flow-control technology, a failure in the active flow control elements of the system places no operability demands on the engine's compression system because of the presence of the passive flow control element. Hence, the risk of compromising a mission or a vehicle is substantially reduced using a hybrid flow-control system in comparison to relying on an active, inlet-flow-control system with microjets alone. As a result, the development time and risk

for introducing this new technology into an operational vehicle is significantly reduced compared to that of a system relying solely on active flow control to provide flight-critical operation.

This earlier hybrid flow-control system adapts the inlet flow to tailor the performance of a propulsion system throughout its flight/operational envelope to optimize installed thrust, fuel consumption, operability, or life. Boeing's in-house testing with this system has clarified the flow physics of the elements and demonstrated the potential of a hybrid system. This earlier hybrid flow-control system has undergone wind tunnel testing to verify its performance. The technology has been transitioned to Boeing's advanced projects.

The hybrid flow-control system under development in this program goes substantially beyond the earlier system. Here the hybrid system is composed of integrated microvanes and synthetic jets. Microvanes were selected for this study based on their proven effectiveness in controlling secondary flows in offset diffuser designs required for HWB aircraft with embedded engines. Furthermore, the use of synthetic jets, in lieu of microjets, will result in less fuel burn. No bleed-air extractions will be used with the synthetic jets and bleed air ducting and control systems will not be needed. This approach facilitates major system level benefits.

Objectives

This program has two key objectives. The first is to develop fail-safe flow-control technologies for highly integrated offset inlets to move towards "N+2" project goals. The second is to develop and improve novel test methods and validate tools for predicting active hybrid flow-control effectiveness in managing inlet pressure distortion. From this program, validated computational tools will be available to improve system trades for advanced inlet concepts. The prediction capabilities will be applicable to a range of subsonic, fixed-wing aircraft, and validated for advanced HWB vehicles. The tools will enable accurate prediction of active hybrid flow-control-system effectiveness in controlling inlet total-pressure distortion at conditions relevant to flight.

The objectives are being accomplished in two phases. In Phase 1, passive, active, and hybrid flow-control devices were used to alter boundary-layer characteristics for improved resistance to separation in the presence of an adverse pressure gradient. CFD was employed in combination with experimental testing to characterize the flow physics of flow-control devices. CFD-based analysis tools for the simulation of active hybrid flow-control devices were developed and validated against test data. The Phase 1 work was completed in Fiscal Year 2008 and detailed in a previous report.

The Phase 2 work is being conducted during Fiscal Years 2009 and 2010. During Phase 2, the flow physics that govern the interaction between passive and active components of hybrid flow-control devices are being investigated. The influence of flow control on inlet performance in an offset duct is being quantified. CFD-based tools developed in Phase 1 are being expanded to simulate active, hybrid flow control in an offset duct and validated against test data.

Approach

Experimental investigations, robust modeling, and numerical simulations comprise the approach employed to accomplish the program objectives. During Phase 1, experimental investigations were conducted in a contoured, 2–D-duct test section of a wind tunnel where the contoured surface was designed to mimic the adverse pressure gradient in an offset diffuser of an advanced hybrid-wing / body vehicle. Flow-control hardware was integrated into the duct wall and used to develop test techniques and evaluate the effectiveness of passive, active, and hybrid flow-control devices in improving boundary-layer characteristics. Detailed flow diagnostics, including high-magnification particle image velocimetry (PIV), were employed to develop an understanding of the flow physics associated with the flow-control actuators. These measurements were used to identify flow control configurations that would likely be effective for controlling secondary flows and flow separation in an offset diffuser, as well as, to validate advanced, numerical-modeling tools. Analytical and response surface modeling approaches were

developed and applied, in conjunction with CFD methods, to simulate the effects of synthetic-jet actuators on a flowfield commensurate with that in the offset diffuser of an advanced hybrid-wing / body vehicle.

Phase 2 builds on the accomplishments of Phase 1 by characterizing the interaction between passive and active flow-control devices, demonstrating diffuser performance benefits of hybrid flow-control devices in an offset diffuser, and developing and validating CFD-based analysis tools for the simulation of hybrid flow-control devices. Benefits of second generation, hybrid-inlet-flow control are being assessed in terms of both inlet performance improvements and vehicle system integration. Response surfaces derived from the flow-control performance databases generated in this program may be used to develop and optimize design guidelines for fail-safe, second generation, hybrid flow-control actuators in an offset diffuser. In addition, the experimental database generated in Phase 2 of this program will provide details necessary to understand the complex physics of applied inlet-flow control and support development of numerical modeling techniques, including hybrid Reynolds-Averaged Navier-Stokes/Large Eddie Simulation (RANS/LES) CFD methods for predicting dynamic pressure distortion.

During the current reporting period, experimental techniques were developed and applied to characterize the complex physics resulting from flow control actuation in an adverse pressure gradient. Results of the experiments were used to validate and improve CFD predictive capabilities. Validated CFD predictive tools were employed to assess the baseline and actuated flow in a Boundary-Layer-Ingesting (BLI) inlet diffuser. In addition, dynamic CFD simulations of an offset BLI-inlet diffuser were conducted in order to assess the capability of using Hybrid-RANS/LES-CFD for predicting dynamic, pressure distortion. Finally, during the current reporting period, the design and fabrication of an offset diffuser was completed in preparation for measuring the effects of flow-control technologies on inlet distortion and recovery in a BLI-inlet diffuser at the Georgia Institute of Technology Fluid Mechanics Research Laboratory (FMRL) transonic facility during year three of this program.

Experimental Setup and Procedures

Experimental tests during this program are being performed in the Georgia Institute of Technology FMRL transonic facility shown schematically in Figure 4(a). This facility is an open return, pull-down wind tunnel. The tunnel uses a 150 hp inverter duty motor capable of pulling 85 in. of water to reach test section speeds of Mach 0.73. The motor is controllable to ~ 0.005 percent speed. Ambient temperatures are maintained by a 20-ton, air-cooled, hermetic-scroll, liquid chiller coupled with an ultra low-pressure-drop heat exchanger. Flow-control investigations are carried out with the tunnel operated in one of two configurations. The flow-control devices are integrated into a profiled wall in the 2–D test section of the tunnel. Following those tests, the 2–D duct will be replaced with an offset diffuser. Flow-control devices will be integrated into the diffuser surface and inlet performance and operability will be assessed.

Profiled, 2–D Duct

The 2–D test section used for the initial flow-control investigations measures 5-in. high by 5-in. wide with a length of 24-in. The modular, upper wall of the test section was modified for the present experiments. Specifically, the flat tunnel wall was replaced with a CD (CD) wall, as seen in Figure 4(c). The adverse pressure gradient on the profiled wall was designed such that the pressure gradient $d(p_s/p_{inf})/dx \approx 0.38$, which is consistent with the pressure gradients in diffusers of HWB vehicles such as the Blended Wing Body (BWB).

During the current reporting period, combinations of passive (microvane or microramp) and active (synthetic jet) flow-control elements were surface mounted near the apex of the CD test-section. Schematic descriptions of the devices are shown in Figure 5, where the streamwise position is measured relative to the wall apex. Diagnostics of the resulting flowfield are done using high-resolution PIV measurements at multiple spanwise (z-direction) “cuts” through the flowfields. The PIV optical setup, Figure 4(b), includes synchronized, computer-controlled, motorized motion of the all of the optics, including the laser, along the test section axial direction and additional motorized motion of the PIV camera in the cross-stream direction.

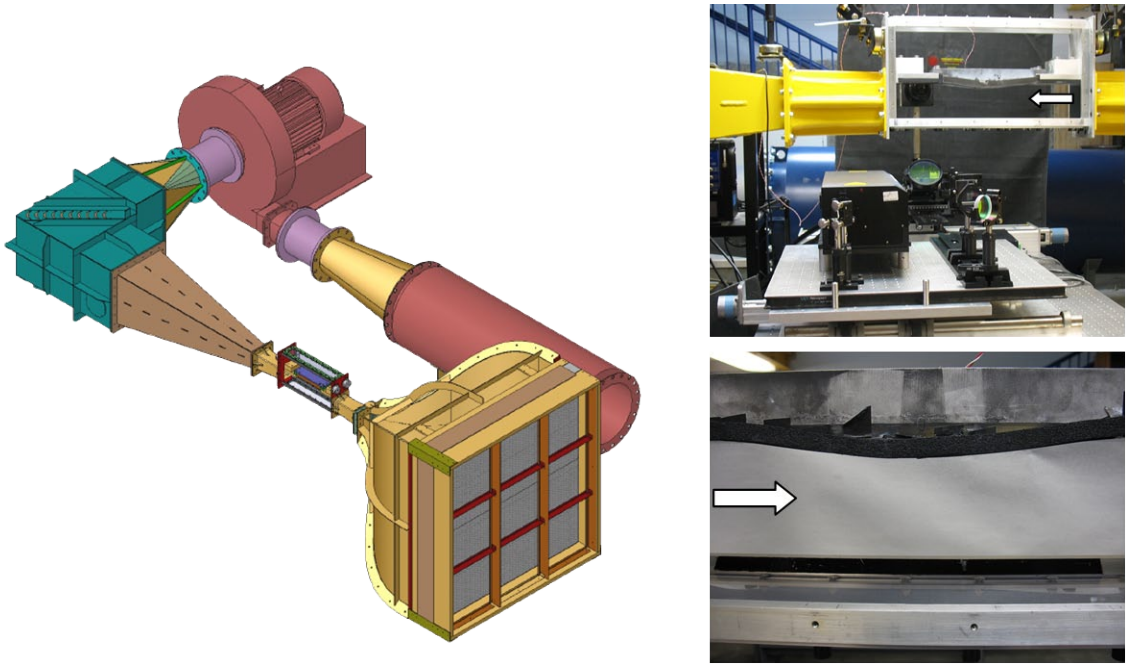

Figure 4.—The Transonic Wind Tunnel (a), test section and PIV optical setup (b), and Profiled upper wall of the test section (c).

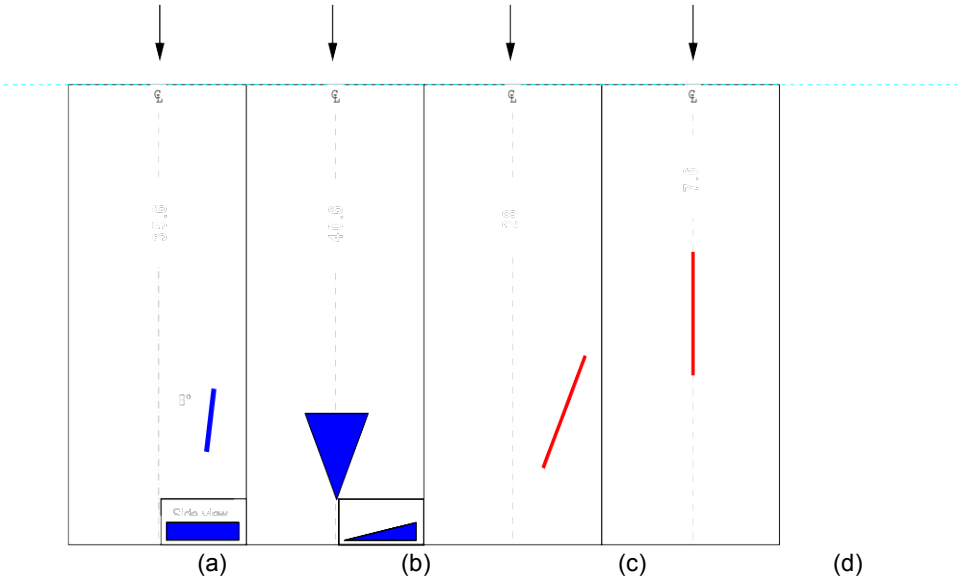

Figure 5.—Flow-control element configurations: (a) microvane, (b) microramp, (c) slanted, (d) streamwise. (The distance of each element from the surface apex is denoted in mm.)

The characteristic scaling of the passive devices employed in the present investigation was defined in terms of the local, boundary-layer thickness, δ. Specifically the sizing guidelines employed were based on design guidelines presented in the statistically designed studies by Anderson et al. (2004, 2006). For a freestream Mach of 0.5, δ measured 0.20 in. (5 mm) at the wall apex. The microvane, Figure 5(a), was designed with a rectangular planform measuring 0.25 δ and 2.56 δ in the cross-stream and streamwise directions, respectively. The microvane was oriented at an angle of 8° relative to the freestream. The microramp, Figure 5(b), measures 0.51 δ high, 3 δ wide, and 3.4 δ long, and has a half-angle of 24°.

In addition to passive devices, active and hybrid devices were examined. The active, synthetic-jet orifice measured 0.98 in. (24.9 mm) long by 0.02 in. (0.5 mm) wide and could operate within the range of 1 to 2.5 kHz. The isolated jet was tested in two orientations, aligned with the freestream, Figure 5(d), and slanted, Figure 5(c). The slanted jet was installed at an angle of 24° to the freestream, which is equivalent to the half angle of the microramps. Both jet configurations blew normal to the surface. The hybrid configurations were comprised of passive devices closely coupled to active devices. Two types of hybrid configurations were examined, those that included microramps as the passive actuator and those that included microvanes. In the microramp hybrid devices, the streamwise-aligned jet was located along the microramp centerline, 0.31 in. (8 mm) upstream of the microramp, Figure 6. In the microvane hybrid configurations, the synthetic jet was slanted at the same angle as the microvane and skewed to blow at an angle in the spanwise direction, which will henceforth be referred to as the skew angle, Figure 7.

Diagnostics employed in the present investigation include high-resolution, high-speed PIV measurements at multiple cross-stream planes of the flowfield. The PIV field of view measured 0.67 in. (17 mm) on the side and the magnification was 17 μm/pixel. The outlines of the PIV measurement stations are shown in Figure 6 (referenced to a hybrid configuration). Near-field measurements were taken at centerspan, marked "1", where the PIV view is comprised of four partially overlapping streamwise fields. Far-field measurements were taken at $x/\delta_{apex} = 42$ downstream of the downstream edge of the microramp, at cross-stream planes 0.039 in. (1 mm) apart.

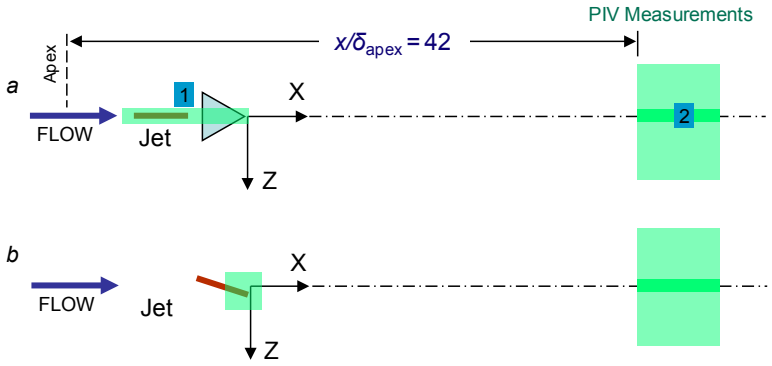

Figure 6.—Schematics of the PIV measurement domains for (a) hybrid flow control and (b) slanted-jet active flow control.

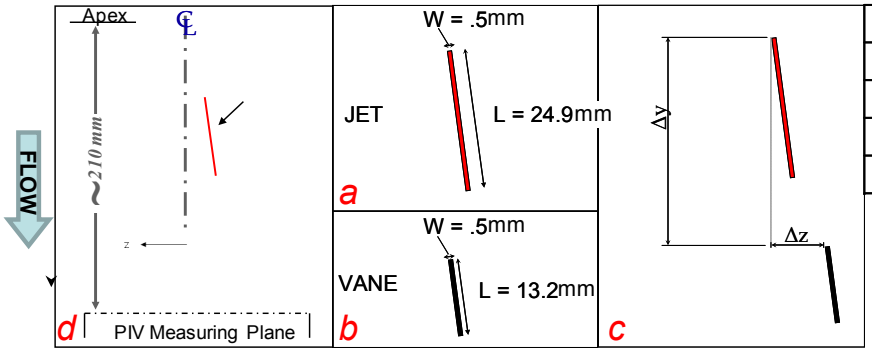

location		Δy [mm]	Δz [mm]
downstream	v1	37.2	-0.5
downstream	v2	37.2	7.5
downstream	v3	37.2	-8.6
downstream	v4	37.2	2.8

Figure 7.—(a) Synthetic jet and (b) microvane dimensions and (c) relative spacing. (d) location and orientation of PIV measuring station. (Flow from top to bottom of page.)

Offset Diffuser

Following the conclusion of the flow-control device assessments in the 2–D test section, the test section will be removed and replaced with an offset duct that was designed to be consistent with future HWB vehicles. Design and fabrication of this duct was conducted during the current reporting period. The replacement hardware utilizes the existing contraction, diffuser, and drive system of the Georgia Institute of Technology FMRL transonic wind tunnel to provide the airflow requirements for the duct system. This facility was designed to be suspended from an overhead beam system, allowing for vibration isolation and a limited adjustability of the component locations. In order to account for the diffuser offset and slightly shorter overall length of the IFCPT assembly, the contraction was moved approximately 2.5 in. downstream, and approximately 5.2 in. to one side. This, along with the adjustability of the support struts suspending the facility, were sufficient to mate the new hardware to the existing hardware.

The offset-duct-model apparatus consists of a forward adapter, BLI S-duct, AIP total pressure rake assembly, and the aft adapter, Figure 8. The Forward Adapter serves as the transition between the existing facility contraction and the offset duct. It also contains a provision for mounting a boundary-layer fence. The diffuser-assembly moldline was defined based on the current BWB diffuser moldline. The duct model was designed with a removable insert in the lower surface to provide for installing and testing flow-control devices. Two sets of contoured windows were incorporated into the design to facilitate the acquisition of PIV data. Three hot-wire installation locations were also included near the duct throat. Finally, the aft adapter serves to mate the AIP to the existing facility expansion section.

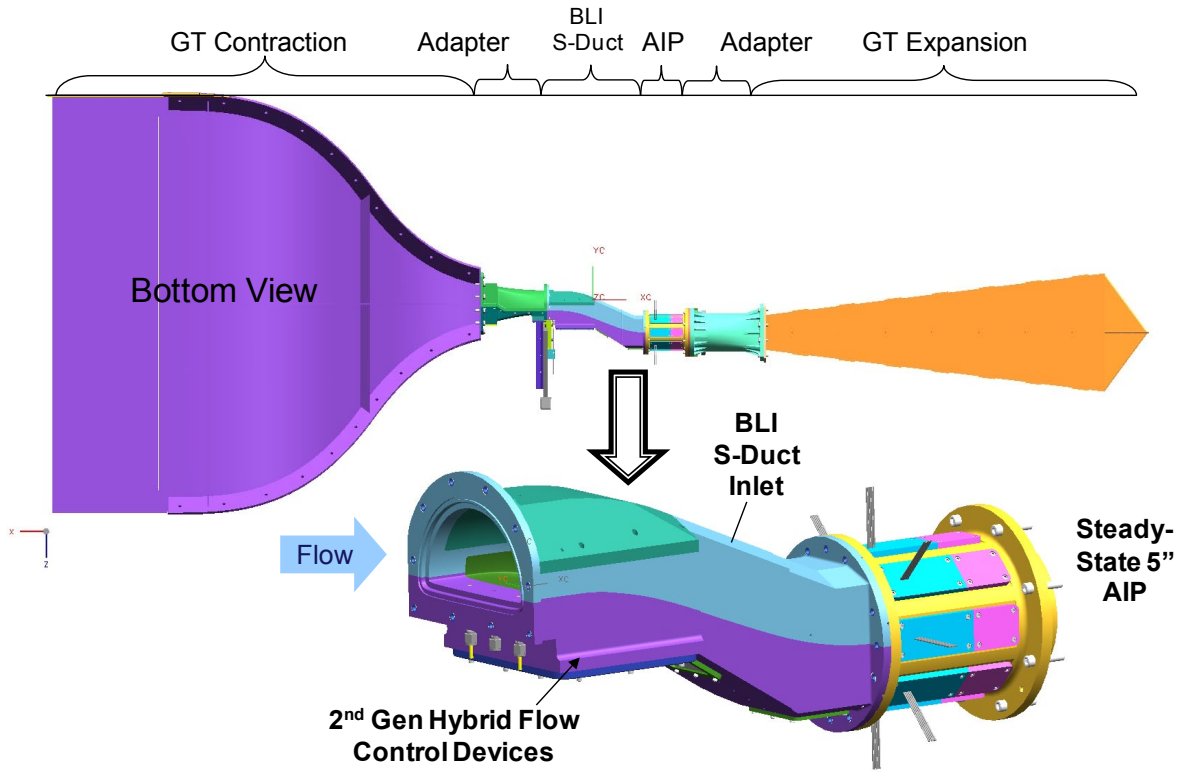

Figure 8.—BLI offset diffuser model.

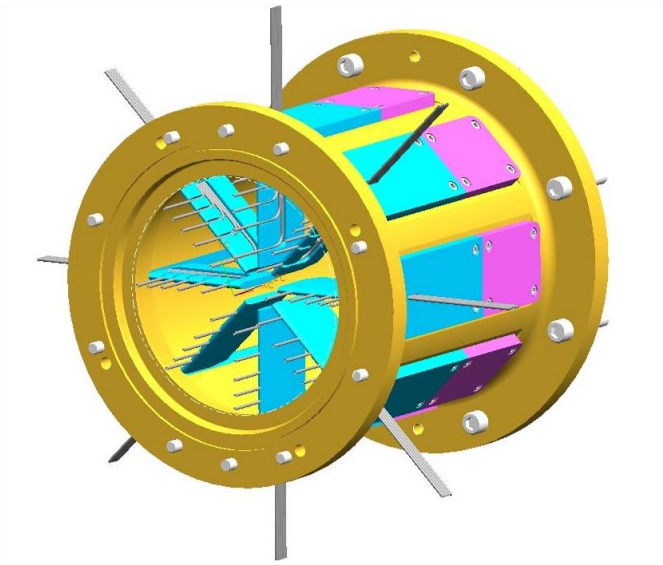

Figure 9.—AIP total-pressure rake assembly.

Instrumentation on the model includes twenty-one static-pressure taps on the inner-moldline surface. In addition to the static taps, the model includes a steady-state total-pressure rake assembly, Figure 9, which consists of eight equiangularly spaced rakes around the circumference of the AIP. Each rake contains five total pressure probes located at the centers of equal areas. The rake assembly was designed such that the eight steady-state rakes would be interchangeable with existing, Boeing-owned, dynamic-total-pressure rakes for the acquisition of dynamic distortion data.

Numerical Simulation Technique and Flow Conditions

In addition to experimental facilities and hardware, state-of-the-art numerical methods were employed to develop and validate prediction tools for inlet flow-control-technology development. To accomplish this, steady and unsteady numerical simulations of flow in the Georgia Institute of Technology FMRL transonic tunnel test section, as well as, in offset diffusers were generated. The Boeing Computational Fluid Dynamics (BCFD) code was used for the numerical simulations. In all cases, the 3–D viscous Navier-Stokes equations were solved in the domain of interest. Both structured and unstructured grids were used to represent the computational domains. The Boeing Modular Aerodynamic Design Computational Analysis Process (MADCAP) tool was used to generate the surface mesh. For the unstructured grids, Advancing-Front/Local-Reconnection (AFLR) was used to generate the interior volume mesh. Mesh spacing were taken from a grid resolution study of BLI-inlet simulations conducted in Phase 1 of this program, as well as, additional grid-resolution studies of the FMRL tunnel test section. The Roe flux-differencing numerical discretization scheme was used on the governing equations in the structured grid zones, while the Harten-Lax-van Leer-Einfeldt (HLLE) flux vector-splitting scheme was applied in the unstructured zones. Two turbulence models were used in the simulations. The one-equation Spalart-Allmaras (SA) model was used in a limited number of dynamic distortion simulations, while the two-equation Shear-Stress-Transport (SST) model was used for the majority of the simulations.

For simulations in the offset duct, constant-pressure boundary conditions were prescribed downstream of the AIP in order to control the duct mass flow. The Mach number at the throat for all cases comparing flow control and dynamic distortion was maintained at approximately 0.7, which corresponds to a corrected mass flow of approximately 5.5 lbm/s at the AIP.

Results and Discussion

Experimental Characterization of Flow-Control-Device Physics

In support of the program objective to develop flow-control technologies, the interaction of surface-mounted, passive and active flow-control devices with the cross flow was examined both experimentally and numerically during the current reporting period. The experiments were conducted in a small-scale wind tunnel at high subsonic speeds of up to Mach 0.5. Numerical simulations were carried out using the 3–D, viscous, Navier-Stokes CFD code, BCFD. The evolution of streamwise vortices induced by the flow control was investigated in an adverse pressure gradient that mimics the pressure gradient within a diffuser compatible with future hybrid-wing/body vehicles. Counter-rotating vortex pairs and single-sense vortices were formed and characterized using passive microramps and microvanes, respectively. Similar streamwise vortices were also generated using synthetic jet actuators. The jets had rectangular orifices that were either slanted and/or skewed to produce single-sense vortices or streamwise aligned to produce vortex pairs. Finally, hybrid actuation approaches were characterized by combining a passive microvane and synthetic jet in a tandem arrangement.

Passive Flow-Control Devices

The single-sense and counter-rotating, streamwise vortices induced by microvanes and microramps were characterized in the adverse pressure gradient domain downstream of the test-section-wall apex, Figure 4(c). The initial vortex formation from the passive elements was investigated through surface oil visualization using a mixture of linseed oil and titanium-dioxide paint. The oil traces around the microvane, Figure 10(a), indicate stagnation points upstream and downstream of the microvane leading and trailing edges, respectively. The pressure differential across the microvane surfaces resulted in the rollup of a "tip vortex", which rolls to form a single-sense, streamwise vortex. The oil-streak accumulation downstream from the trailing edge of the microvane indicates roughly an upwash region across the boundary layer. Figure 10(b) shows the near-wall topology of the flow over the microramp and initial vortex formation. A symmetric split of the oncoming flow over the microramp is visible, and the footprint of the initial streamwise roll of the flow is evident from the wall traces on each side of the microramp. As more fluid rolls into each streamwise vortex that forms along the microramp edge, its footprint on the microramp sidewall intensifies. The evolving counter-clockwise (CCW) and clockwise (CW) vortices, in the downstream view, that form along the left and right edges of the microramp, respectively, merge at its tip and are advected downstream within the boundary layer This is evident from the two narrow traces about the microramp axis. These traces are not a normal projection of the vortex cores. They delineate the upwash due to the vortex-induced, spanwise flow. The vortex pair self-advects away from the surface as is evidenced by the streamwise thinning of the upwash traces. Nevertheless, the streamwise flow clearly dominates the way in which the vortex pair is convected downstream.

The far-field effect of the microramp on the boundary layer at $x/\delta_{apex} = 42$ is elucidated from a sequence of planar PIV measurements in cross-stream planes, at a number of spanwise stations, Figure 6(a). A color raster plot with contours of composite, time-averaged, streamwise and cross-stream velocity distributions in the y-z plane are shown in Figure 11(a) [$U(y,z;x)$] and Figure 11(b) [$V(y,z;x)$], respectively. In addition, contours of the streamwise velocity difference, in the presence and absence of the microvane, are shown in Figure 11(c). The raster plots illustrate the effects of the flow-control device with contours of composite, time-averaged, streamwise and cross-stream velocity distributions in the cross-stream (y-z) plane at $x/\delta_{apex} = 42$. Note that the cross-stream (z-y) plane in the raster plots is viewed in the upstream direction. The distributions in Figure 11 indicate a clear upwash effect at center span (the centerline of the microramp) which is accompanied by the downwash domains with peaks at $z/\delta_{apex} = +1$ and –1 on both sides of the upwash. These effects are a direct consequence of the counter-rotating-vortex pair induced by the microramp. To better isolate the effect of the streamwise vortex, the streamwise velocity increment and decrement relative to the baseline, non-actuated flow, $\Delta U(y,z;x)$ is shown in

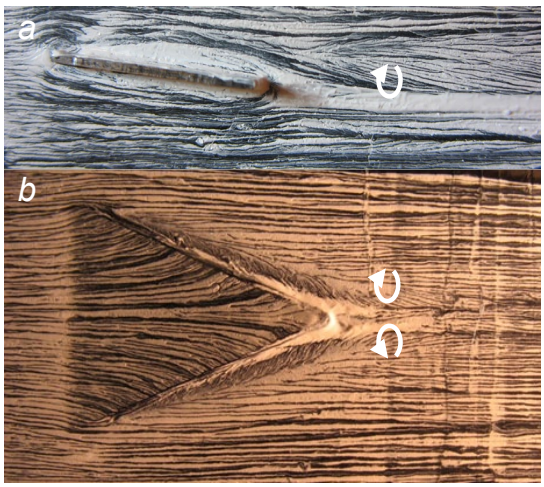

Figure 10.—(a) Surface oil-flow visualization of the streamwise single-sign and (b) vortex pair formation.

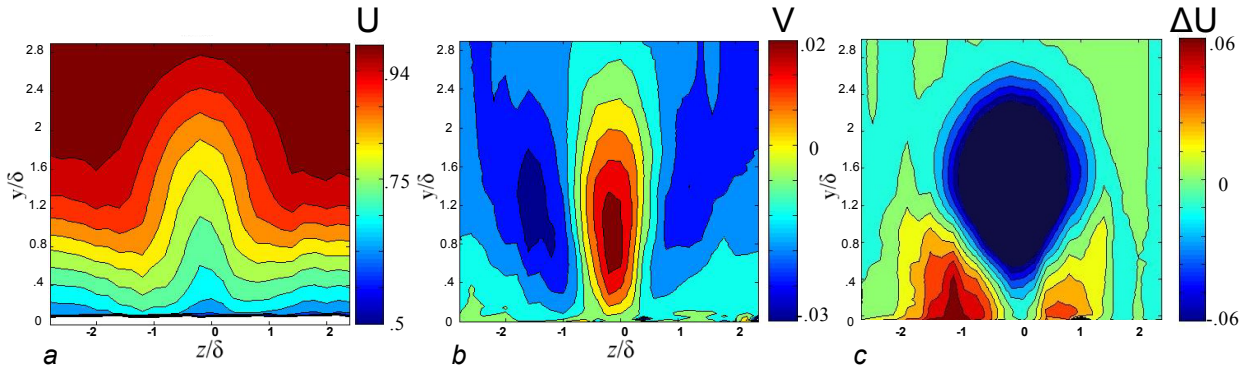

Figure 11.—Color, raster, composite, time-averaged contour plots at x/δ_{apex}= 42 downstream of the microramp of (a) streamwise velocity, U, (b) cross stream velocity, V, and (c) streamwise velocity difference from baseline.

Figure 11(c). Inspection of Figure 11(c) indicates that the deficit caused by the common upwash of the vortices is advected upward introducing higher speed flow in the near wall region. The slight bias in the PIV measurements, in which the boundary layer appears slightly inclined in the absence of the microramp is caused by a slight misalignment between the PIV camera horizon and the wall contour.

A cross-stream integral effect of the microramp on the boundary layer flow was assessed from the relative spanwise changes in the shape factor, *h,* of the cross-stream velocity distribution in the absence and presence of the microramp, Figure 12. These data show that the spanwise extent of the microramp is almost $5\delta_{apex}$, while the microramp width is about $3\delta_{apex}$. The most prominent feature of the boundary-layer shape factor is that the induced, streamwise vortices lower the shape factor through most of the affected spanwise domain. Even though the upwash along the centerline of the microramp increases the boundary-layer-velocity deficit, Figure 11, the vortex pair is sufficiently far from its source, such that its lift off the wall actually leads to a decrease of the velocity deficit near the wall. In the downwash region, the transport of high-momentum fluid towards the surface leads to an increase in the velocity deficit near the wall. The combination of off-centerline downwash and displaced upwash in between is what makes the microramp attractive (when properly scaled) for boundary layer separation delay (Lin, 2002).

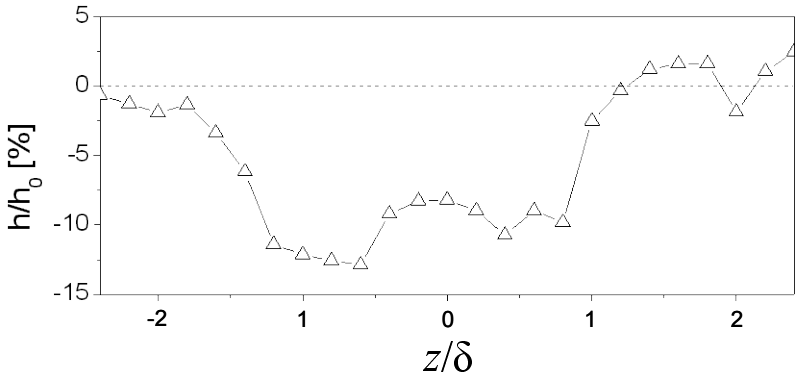

Figure 12.—Spanwise distribution of the boundary-layer shape factor, h, downstream of the microramp at x/δ_{apex}=42 normalized by the baseline shape factor, h_0.

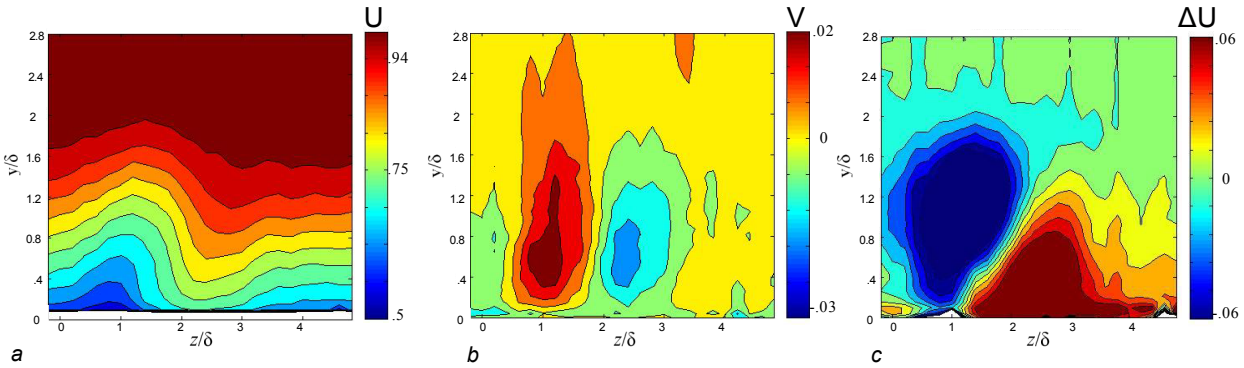

Figure 13.—Color, raster, composite, time-averaged contour plots at x/δ_{apex} = 42 downstream of the microvane of (a) streamwise velocity, U, (b) cross stream velocity, V, and (c) streamwise velocity difference.

Similar to Figure 11, the changes in the flowfield that are induced by a microvane were measured at x/δ_{apex}=42 and are shown in color raster plots, Figure 13(a) and Figure 13(b). The time-averaged distribution of the streamwise velocity $U(y,z;x)$, Figure 13(a), shows the upwash ($0.5 < z/\delta_{apex} < 2$) and downwash ($2 < z/\delta_{apex} < 3$) domains, indicating the presence of a CW streamwise vortex. This is further supported by the distribution of the cross-stream velocity, Figure 13(b), that includes two adjacent zones of fluid motion either away (upwash) or towards (downwash) the wall. As might be expected, owing to the presence of the wall, the cross-stream elevations of the peaks (positive and negative) of ΔU, Figure 13(c), are different. The deficit owing to the upward advection of low-momentum fluid at $y/\delta_{apex} \approx 1.2$ is farther away from the surface than the high-momentum fluid at $y/\delta_{apex} \approx 0.4$. In fact, the transported high-momentum concentration appears to spread in the spanwise direction along the surface. It is noteworthy that the upwash in absence of an opposite-sense vortex is not sufficient to displace the low momentum fluid away from the surface indicating that the effectiveness of the microvane in terms of overcoming flow separation may be lower than that of the microramp.

This is further confirmed by the distribution of the shape factor $h(z)$ across the span, Figure 14. In comparison to the corresponding distribution for the microramp, the domain in which $h(z)$ increases is considerably broader. However, considering that the spanwise projection of the microvane is approximately $0.4\delta_{apex}$, compared to $3\delta_{apex}$ for the microramp, perhaps comparable effects can be achieved by increasing the packing density of the microvanes.

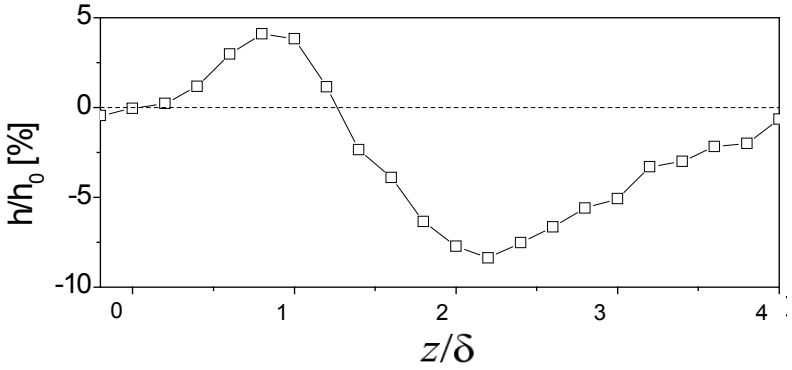

Figure 14.—Spanwise distribution of the boundary-layer shape factor, h, downstream of the microvane $x/\delta_{apex} = 42$ normalized by the baseline shape factor, h_0.

Active Flow-Control Devices

In addition to passive devices, active synthetic-jet flow-control devices were tested to compare the effectiveness of the different types of actuation in forming controlled counter-rotating or single-sense, streamwise-vorticity concentrations. Isolated, synthetic jets were tested in two orientations, streamwise aligned and slanted, relative to the freestream flow. The streamwise aligned configuration was designed to produce vortical structures consistent with microramp actuation, while the slanted jet was designed with the intent of producing structures consistent with microvane actuation.

As expected, aligning the long dimension of the rectangular, jet orifice with the direction of the free stream, as illustrated in Figure 5, produced a pair of counter-rotating, streamwise vortices. In still air, the counter-rotating vortices were generated along the orifice at each actuation cycle. In the presence of a cross flow, the vortices were augmented by the tilting and rollup, predominantly in the spanwise direction, of boundary-layer vorticity and often loosely connected at their downstream end, similar to a lambda vortex. The vortices, which were advected with the local cross flow, were interrupted and vanished during the suction stroke. Because the strength of the streamwise vortices that are formed by a synthetic-jet actuator is streamwise modulated with the periodicity of the actuation, the time-averaged vortex strength is considerably weaker than the instantaneous strength. A streamwise, vortex pair induces an upwash along its common axis and a downwash off centerline. The resulting changes in the baseline flow are shown in Figure 15 using color raster plots of the time-averaged streamwise and cross-stream velocity components. As expected, when the streamwise jet was active, Figure 15(a), there was a noticeable upwash near the centerline peak in boundary layer thickness. The peak is flanked on either side by weaker downwash where the high-speed flow was drawn closer to the wall. Analogous to Figure 11(c), the distributions of the streamwise velocity differences relative to the unforced flow, $\Delta U(y,z;x)$ are shown in Figure 15(c). These data indicate that the time-averaged flow induced by the synthetic jet was qualitatively similar to the far-field structure of the flow induced by the microramp. The corresponding shape factor, Figure 16, indicates that the streamwise jet led to an overall decrease in the shape factor, but the magnitude of the decrease was smaller than that induced by the microramp. Since the jet-orifice orientation is fixed, the jet momentum, or impulse per stroke, controlled the strength of the induced streamwise vortices. However, in this case, for a fixed jet velocity, the characteristic, spanwise scale of the jet also impacted the strength of the ensuing streamwise vortices. In the present configuration, the spanwise domain of influence of the jet was approximately $5\delta_{apex}$, which was similar to that of the microramp. However, the spanwise width of the jet was about 30 times smaller than that of the microramp or $0.1\delta_{apex}$ compared to $3\delta_{apex}$.

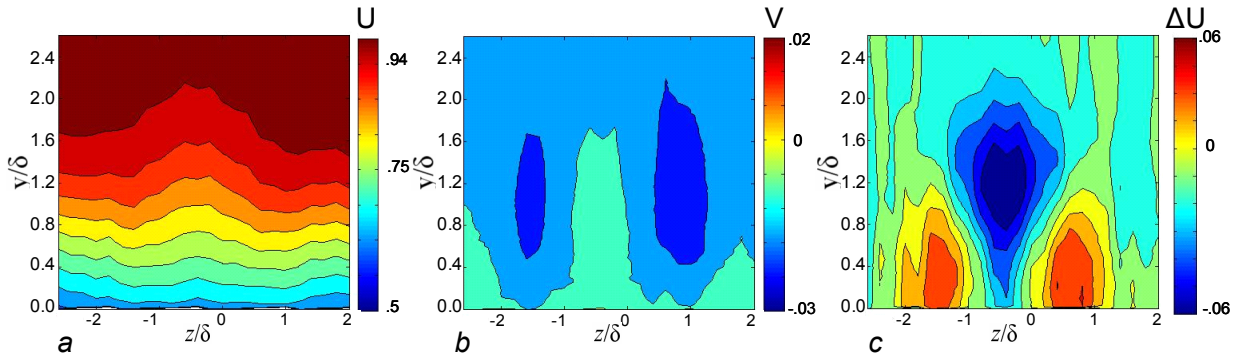

Figure 15.—Color, raster, composite, time-averaged contour plots at x/δ_{apex} = 42 downstream of the streamwise synthetic jet of (a) streamwise velocity, *U*, (b) cross stream velocity, *V*, and (c) streamwise velocity difference.

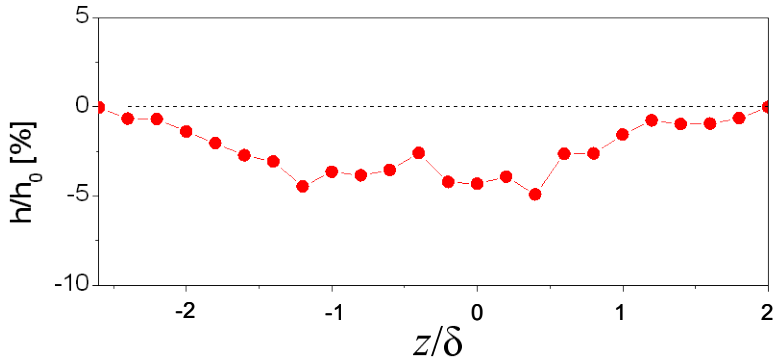

Figure 16.—Spanwise distribution of the boundary-layer shape factor, *h*, downstream of the streamwise synthetic jet x/δ_{apex} = 42 normalized by the baseline shape factor, h_0.

Unlike the streamwise-aligned jet, slanting the orifice of the jet, relative to the free stream, in the orientation shown in Figure 5(c) produced a single, streamwise vortex. The jet-slant angle was the same as the half angle of the microramp. The resulting flow in the far field, Figure 17, indicates the presence of a CCW-streamwise vortex. Unlike the streamwise jet, the low-speed flow that was pushed out away from the wall, was not convected upward quite as strongly, which led to areas of both increased and decreased velocity deficits in the near-wall region, as also illustrated by the raster plot of the velocity difference in Figure 17(c). Although the synthetic jet was slanted at the same direction as the microvane, as shown in Figure 5, they generated single, streamwise vortices of opposite sense. Specifically, the vortex formed by a microvane is similar to a tip vortex of a lifting surface. However, the vortex that is formed by the jet appears to roll as a result of the bending of the jet by the cross flow, as shown by Peake et al (1999) for continuous, conventional jets. This result is also consistent with the measurements of Compton and Johnson (1992) for skewed jets.

The near-field formation of the vortex that was generated by the slanted jet was measured in 16 cross-stream (*y*-*z*) planes spaced 0.039 in. (1 mm) apart, where the field of view measured 0.669- by 0.669-in. (17- by 17-mm). The measurement region began at x/δ_{apex} = 2 downstream of the upstream orifice edge, Figure 6. The resulting rendition of a 3–D composite of near-field flow is shown in Figure 18. Figure 18(a) shows surfaces of the cross-stream velocity. The presence of the jet forces the oncoming flow up away from the surface along the jet orifice and induces a downward flow in a domain that is outboard and downstream from the jet orifice. The bending of the jet by the cross flow is evident in surfaces of the streamwise velocity difference, relative to the baseline flow, Figure 18(b). This phenomenon is accompanied by an increase in the streamwise velocity on the right, downstream of the

orifice, and a small decrease owing to the flow turning on the left. Clearly, the differences in the sense of the streamwise vortices that are formed by slanted, passive obstructions and by similar-slant, synthetic jets must be taken into consideration in the design of hybrid actuators that are comprised of both elements.

The spanwise distributions of the changes in the shape factor affected by the slanted jet are shown in Figure 19. The spanwise extent of the changes in shape factor that are induced by the slanted jet and by the microvane, Figure 14 were quite similar at approximately $3\delta_{apex}$ in the far field. The streamwise projection of the microvane into the spanwise plane was $0.4\delta_{apex}$ and the streamwise projection of the jet into the spanwise plane was $2\delta_{apex}$. Furthermore, the magnitude of the effect of the jet was only about 15 percent lower based on the averaged change in shape factor.

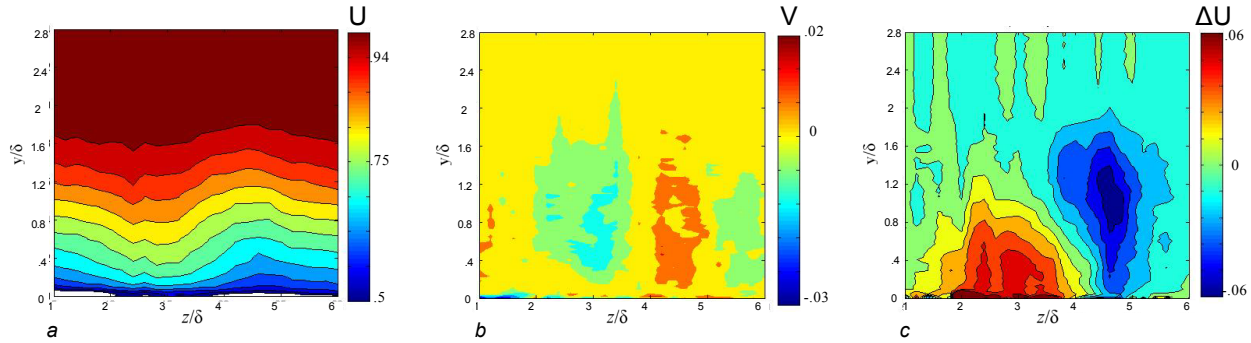

Figure 17.—Color, raster, composite, time-averaged contour plots at x/δ_{apex} = 42 downstream of the slanted, synthetic jet of (a) streamwise velocity, *U*, (b) cross-stream velocity, *V*, and (c) streamwise velocity difference.

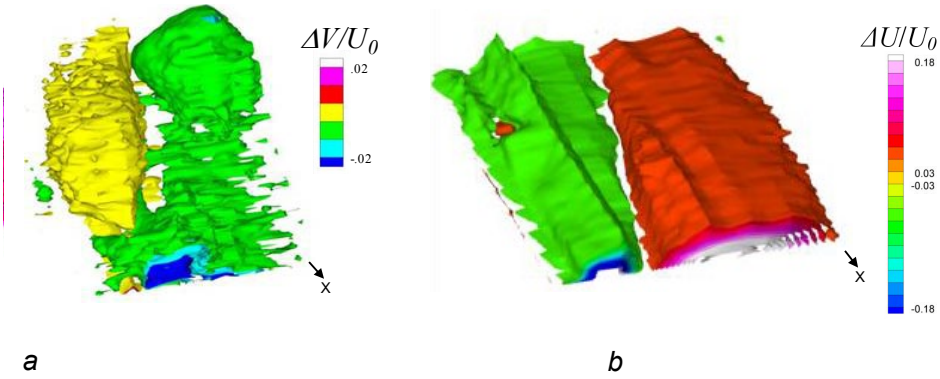

Figure 18.—Composite, upstream view, 3–D, time-averaged velocity field downstream of the slanted, synthetic jet showing surfaces of (a) *V* and (b) Δ*U*.

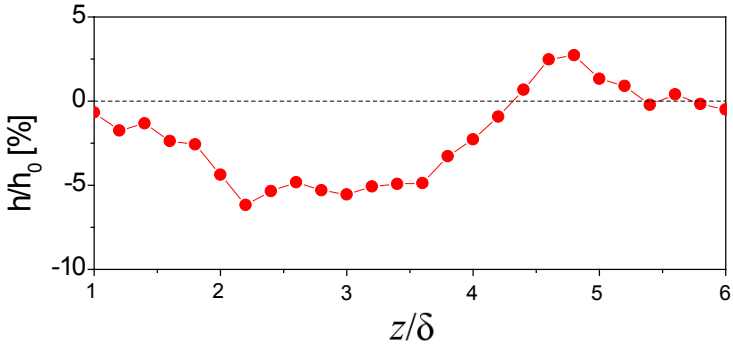

Figure 19.—Spanwise distribution of the boundary-layer shape factor, *h*, downstream of the slanted, synthetic jet x/δ_{apex}=42 normalized by the baseline shape factor, h_0.

Hybrid Flow-Control Devices

Following the exploration and documentation of the governing physics of isolated, passive and active devices operating in a Mach 0.5, adverse pressure gradient flow, the performance benefits attained by adding an active component to a passive flow-control approach was investigated. Hybrid devices were tested to characterize the interaction between closely coupled, passive and active devices. Tests of a hybrid actuator, comprising a vortex generator and synthetic jet, were conducted using a streamwise jet, placed upstream and along the centerline of a microramp, Figure 6(a). This configuration was selected based on the successful integration and purported effectiveness of a hybrid device made up of a conventional, continuous jet and a microramp by Anderson et al. (2009). In addition, hybrid configurations whose components included microvanes and synthetic jets were examined, and performance sensitivities to variations in the device geometric parameters, such as the relative placement and orientation of the microvane and jet were measured and documented.

The flow physics resulting from actuating the flow with a microvane/synthetic-jet hybrid device were investigated. The far-field effects of an isolated microramp were discussed in a previous section, Figure 11. Performance enhancements due to the incorporation of a synthetic jet with a passive microvane were assessed by comparing distributions of the time-averaged, streamwise and cross-stream velocities downstream of the microramp, in the absence and presence of the jet, Figure 20. These data clearly show the central upwash domain and two downwash regions on either side. In addition, these data indicate that the time-averaged effect of the jet in this configuration was somewhat limited in that there was only a slight enhancement of both the upwash and downwash. The spanwise effect of the hybrid actuation was assessed based on spanwise distributions of the shape factor, Figure 21. These data show that the percent of additional changes in the shape factor, relative to the shape factor in the presence of an isolated microramp, are somewhat smaller than the percent changes induced by the jet alone, Figure 12.

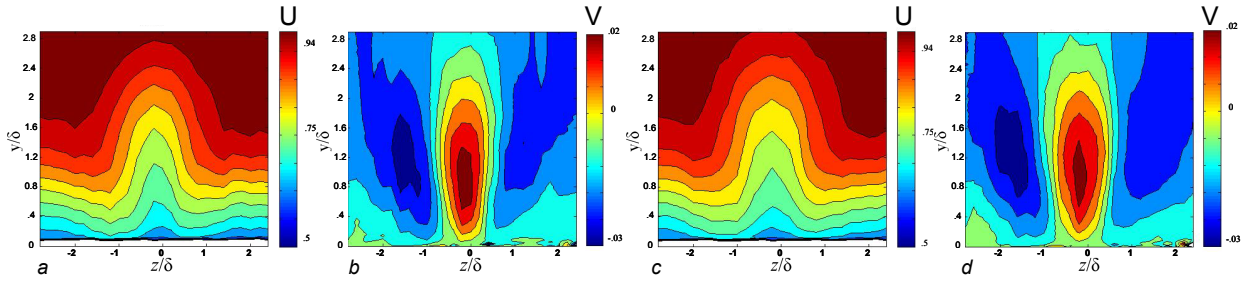

Figure 20.—Color, raster, composite, time-averaged contour plots at x/δ_{apex} = 42 downstream. (a) streamwise velocity of isolated microramp, (b) cross-stream velocity, *V* of isolated microramp, (c) streamwise velocity of hybrid microramp/synthetic jet, (d) cross-stream velocity, *V* of hybrid, microramp/synthetic jet.

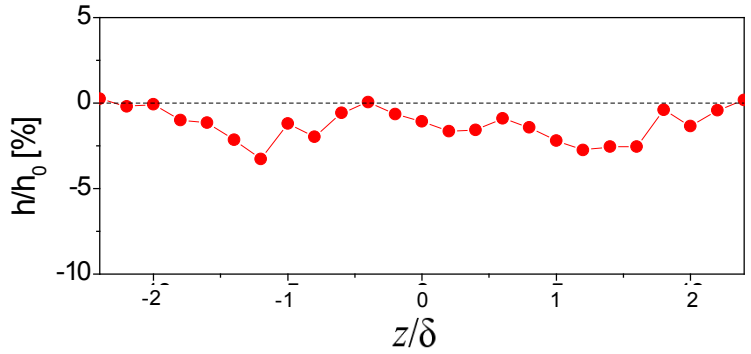

Figure 21.—The shape-factor distribution for the hybrid control (*h*) relative to the passive (h_0) control across the span in the far-field domain (Figure 6(a)).

In addition to hybrid devices comprised of synthetic jets and microramps, synthetic jet/microvane hybrid devices were examined. In the preceding section, it was illustrated that a synthetic jet emerging normal to a surface and slanted at the same direction as the microvane generates single, streamwise vortices of a sense opposite to the microvane, Figure 17. Therefore, in order to facilitate development of a fully integrated hybrid device, the jet orifice was modified such that the jet emanated at a non-zero skew angle, meaning at an angle in the spanwise direction rather than normal to the surface. Various relative positions and orientations of the microvane and synthetic jet were tested to assess performance sensitivities to these parameters. Schematic descriptions of the various devices used in this study are shown in Figure 7, where the streamwise position is measured relative to the wall apex. A nominal microvane at an angle of 8°, Figure 7(a), has a rectangular planform measuring 0.059- by 0.602-in. (1.5- by 15.3-mm) in the cross-stream and streamwise directions, respectively, relative to the free stream. The resulting skewed jet is also slanted with respect to the flow.

The slanted, skewed jet produced a single-sign vortex causing a disturbance in the streamwise component of the velocity, as seen in the far-field composite raster plots, Figure 22. Coherent regions of upwash and downwash are visible in Figure 22(a) and Figure 22(b), respectively. Such a disturbance induces a decrease in the velocity deficit near wall, as visible in Figure 22(c), which shows the difference between the resulting flow and the baseline, uncontrolled flow. The effect of the skewed, slanted jet on the baseline flow was comparable to that of an isolated microvane in a cross flow, Figure 13. Determination that a skewed and slanted jet orifice can generate the same-sense, streamwise vorticity as a parallel microvane enables utilization of a synthetic jet to enhance the performance benefits of a microvane.

The sensitivity of the strength of the single-sense vorticity that results from skewed and slanted-jet actuation was studied by varying the slant angle for a constant skew angle, Figure 23. When the synthetic-jet orifice was aligned with the flow, Figure 23(b), a single-sign vortex was formed. The sign of the vortex was determined by the direction of the skew angle of the orifice. As the jet is slanted at a nonzero angle, the spanwise projection of the orifice increases, and the induced vorticity gives rise to its spanwise component. A small, positive, slant angle slightly increases the far-field area of influence and somewhat enhances the decrease in velocity deficit, Figure 23(a). As the orifice slant angle was increased in the opposite direction, a clear trend of increased area of influence and decreased effect magnitude was measured, Figure 23(c) to (e). Based on this study, the jet orifice, slanted at the same angle as the microvane, was selected for further studies, due to the significant, far-field effect and convenience for any interlaced integration of the jets and the microvanes in a hybrid-control element.

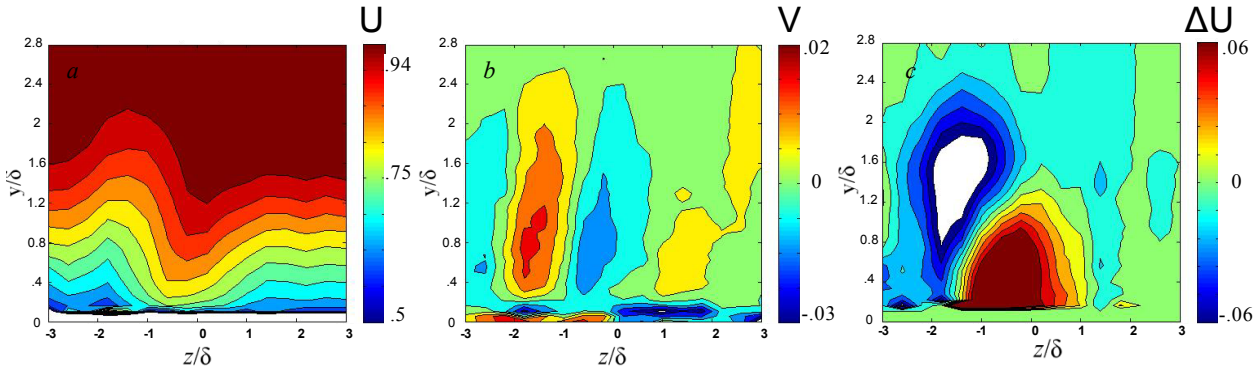

Figure 22.—Color, raster, composite, time-averaged contour plots at x/δ_{apex} = 42 downstream of the skewed, slanted, synthetic jet of (a) streamwise velocity, *U*, (b) cross-stream velocity, *V*, and (c) streamwise velocity difference.

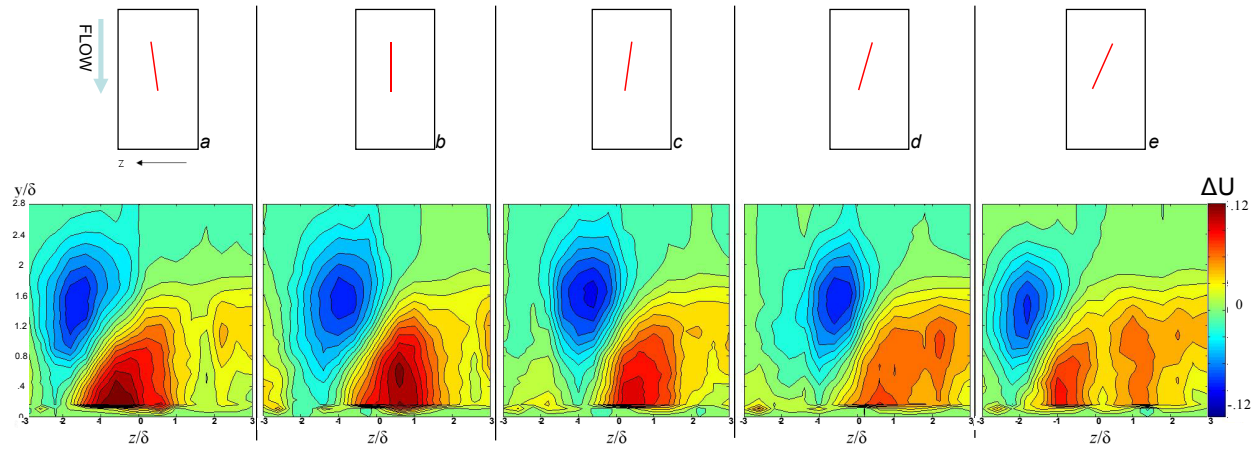

Figure 23.—Contours of the streamwise velocity difference (in the presence and absence of the synthetic jet) are shown for slant angles of: (a) 8, (b) 0, (c) –8, (d) –16, (e) –24.

Following selection of the microvane hybrid device fluidic component configuration, the skewed, slanted, synthetic jet, the passive and active devices were installed in tandem, as a hybrid device, to examine the resulting flow physics in detail. Experiments were performed with the microvane located both upstream and downstream of the jet and in various, relative spanwise locations to provide insight into the nonlinear superposition of the two, distinct, resulting flowfields. Distributions of the time-averaged, streamwise and cross-stream velocities, U^* and V^*, downstream of the microvane, in the absence and presence of the jet, for various upstream spatial locations of the microvane, Figure 24, were used to assess the performance of the hybrid devices. As the microvane was moved in the positive spanwise direction, the resulting vortex that formed off the microvane shifted within the measured field of view, Figure 24. Analyses of the vortices induced by actuation from hybrid configurations at various spanwise spacing between the microvane and jet also showed that the maximum vortex strength was attained when the spanwise spacing was minimized, Figure 24(a) and c. Aligning the jet with the microvane resulted in slightly reduced vortex strength, Figure 24(b). The least favorable configuration was one in which the spanwise distance between the microvane and jet was maximized, Figure 24(d), where two weakly interacting but distinct vortices were seen under superposition of the jet and the microvane.

One strategy previously shown to counteract flow distortion resulting from significant boundary-layer ingestion is to apply flow control that redistributes the concentrated, low total pressure, boundary-layer flow around the perimeter of the AIP, thus creating a distortion pattern to which engines are typically more tolerant. This result may be achieved by using flow control to generate two, large-scale, counter-rotating vortices that sweep the concentrated boundary layer flow up and around the outer perimeter of the duct. In previous studies (Anabtawi et al. 1999), it has been shown that an array of streamwise vortices must be generated such that they merge into a large-scale vortex downstream of the duct, which requires consideration of the vortex sources, sizes and spacing. It is this prerequisite that often dictates the packing density and number of devices. The use of a hybrid system, in place of a passive system offers the potential of reducing the required number of microvanes, thereby potentially reducing total-pressure losses, maintainability, and supportability issues. To this end, two microvanes were placed in the flow such that the pair of resulting vortices exhibited weak interaction at the downstream measuring plane, Figure 25(a) and (c). This microvane pair was then mated with a synthetic jet, analogous to the configuration illustrated in Figure 22 and Figure 24(a). When the jet was activated the microvane-generated vortices merged into one larger, coherent structure, as indicated by the large domain of influence of diminished velocity deficit, Figure 25(b), and by the cross-stream-velocity component, Figure 25(d), which indicated only one zone of upwash and one zone of downwash.

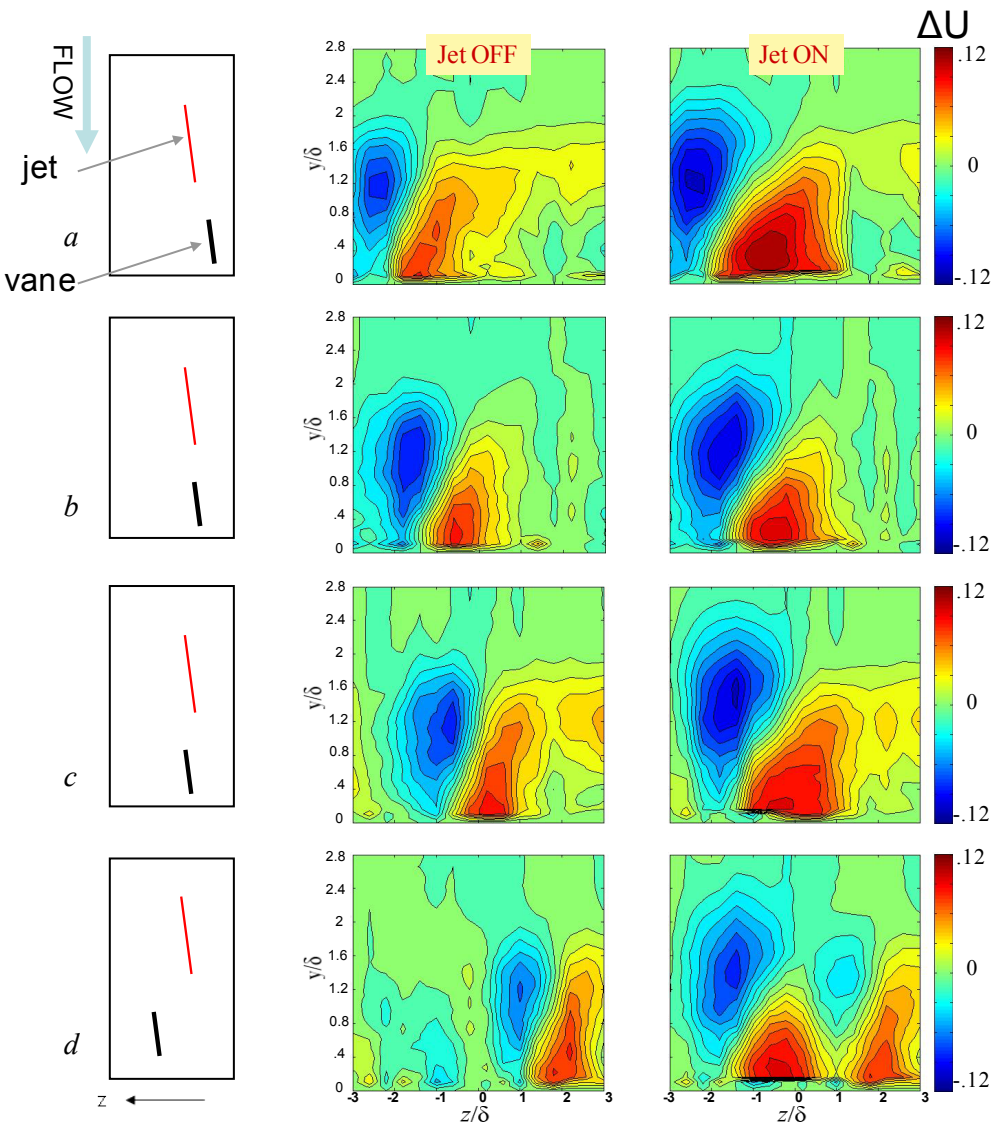

Figure 24.—Contours of the streamwise velocity difference in the presence and absence of the synthetic-jet flow control for various relative spanwise locations of the synthetic jet and microvane.

The integration of a synthetic jet with a pair of microvanes was proven to enhance the weakly interactive vortices resulting from passive microvane actuation. Specifically, hybrid, synthetic-jet/microvane flow control resulted in vortices that merged into one large, coherent structure. These results suggest that implementation of a row of synthetic jets followed by a row of microvanes could be made more efficient by implementing this concept of merging vortices. Furthermore, hybrid microvane/jet devices offer the benefit of reducing distortion with a reduced size and/or number of microvanes, thus offering potential improvements in inlet performance, as well as, system-level requirements such as supportability and maintainability.

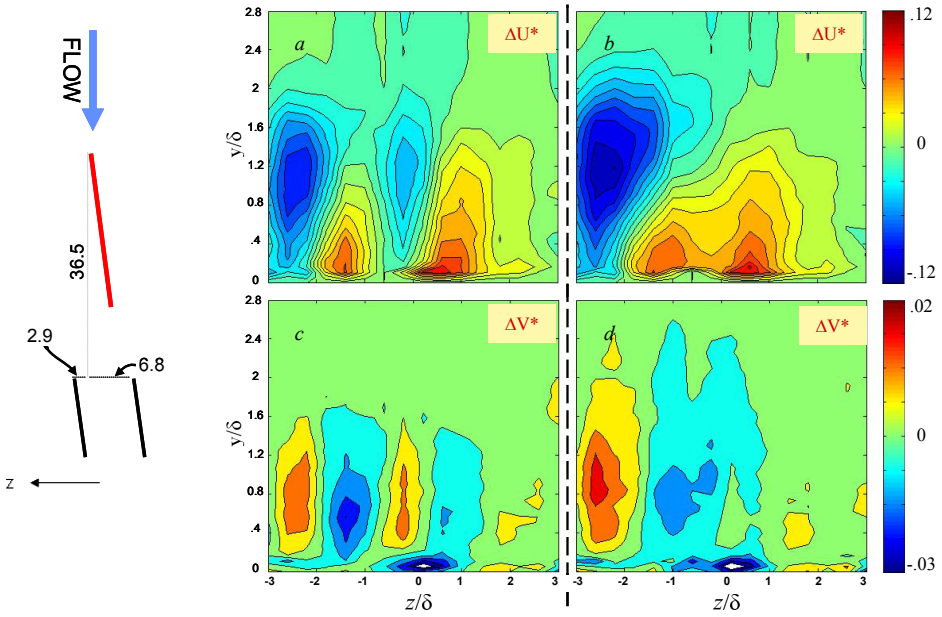

Figure 25.—Contours of the streamwise (a), (b) and cross-stream (c),(d) velocity difference (in the presence and absence of the active flow-control device) are shown for the case where two microvanes are paired with inactive (a), (c) and active (b), (d) synthetic jet.

Numerical Simulations of Flow-Control-Device Physics

As previously stated, a primary objective of this program is to validate tools for predicting active, hybrid flow-control performance. As a step toward meeting that objective, simulations of isolated devices in the Georgia Institute of Technology FMRL tunnel test section with a profiled wall were conducted. Results of the numerical simulations were validated against experimental data detailed in the previous sections. Several factors were varied to explore the sensitivity of numeric results to simulation methodology. These factors included grid resolution, turbulence model, and viscous-flux-calculation technique.

Baseline Wind-Tunnel Simulations

The accuracy of numerical simulations of the baseline wind tunnel flow, in the absence of flow-control devices, was assessed. Specifically, measured and predicted boundary-layer velocity profiles on the profiled wall near the test-section apex were compared, Figure 26. For all figures containing boundary layer profiles, Y_{max} was ~0.69 in. and U_{max} was ~550 ft/s. For all figures containing velocity contours, U_{inf} was ~550 ft/s. The flow approaching the converging/diverging section was at Mach 0.5, standard-day conditions corresponding to the altitude of Atlanta, Georgia. The measured profiles are denoted “GT” in the legend and are plotted at spanwise locations from 1- to 11-mm offset from the centerline. Based on the experimental profiles, the velocity deficit increased monotonically with increasing spanwise offset. This was due to secondary flow, resulting from the sharp corners in the duct imposing an upwash on the otherwise uniform boundary layer.

The numerical simulations were conducted with both SA and SST turbulence models. Both models compared very closely with one another, but the SA model predicted the centerline experimental results slightly better. Away from the centerline, however, the numeric results did not exhibit the same upwash or velocity deficit effect that was realized in the experiment. In fact, the simulated profiles at 1-, 5-, and 11-mm offset fell on top of one another. This suggests that the simulation is not capturing any influence the duct corners have on the flow. It is believed that a significant increase in global grid resolution would be required to capture this effect. Because the offset diffuser does not contain sharp corners, no further

investigation into this was conducted. Nevertheless, the discrepancy was noted for consideration in future simulations.

Passive Flow-Control-Device Simulations

Simulations of the microvane, Figure 27, mounted near the throat of the converging/diverging section of a 5 in. by 5 in. by 30 in. duct representing the test section of the Georgia Institute of Technology FMRL tunnel, Figure 28, were generated and validated against experimental data.

Prior to making comparisons with experimental data, a grid resolution study was conducted to ensure that the grid was sufficiently refined to capture the flow physics. Specifically, the goal was to verify that the simulation accurately predicted the vortex shed by a microvane in an adverse pressure gradient. For each grid refinement level, boundary layer profiles and velocity contours were taken at a station downstream of the throat, Figure 28. These profiles were then compared between refinement levels to determine if the solution was grid independent. A coarse grid consisting of 4.3 million cells and a characteristic surface element size of 0.1 in. served as the starting grid. The method for refinement was to decrease the element size in the wake, Figure 29, downstream of the microvane in order to preserve the vortex strength as it convected downstream.

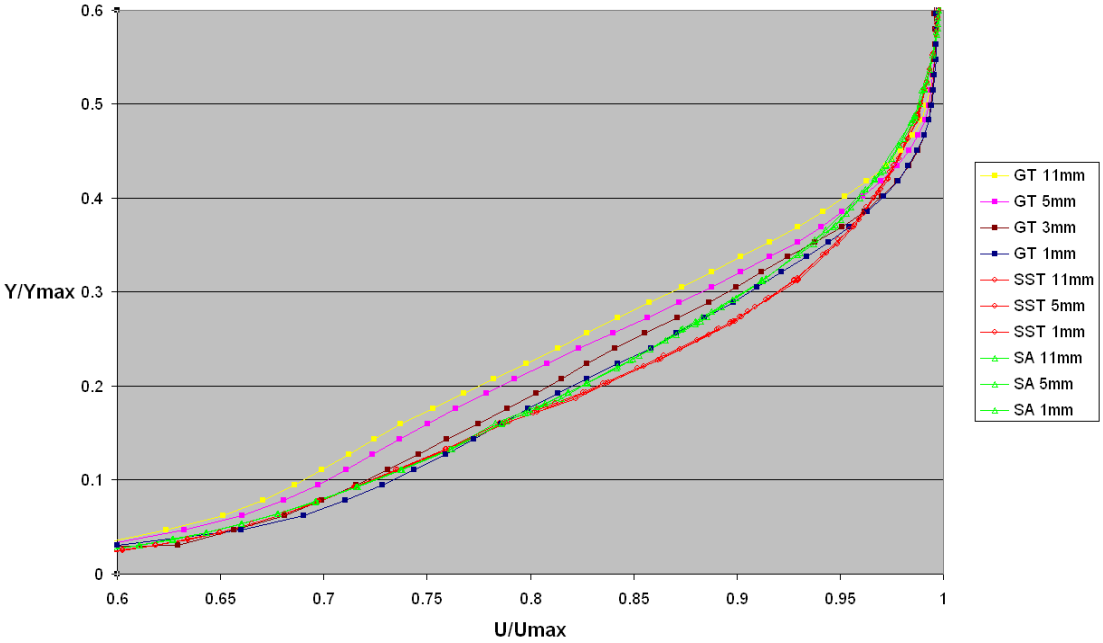

Figure 26.—Baseline comparison of experimental and numerical results.

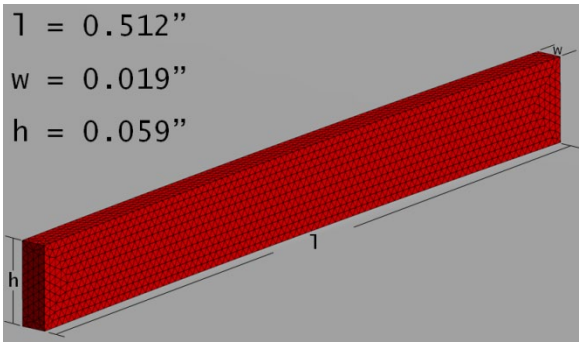

Figure 27.—Microvane dimensions.

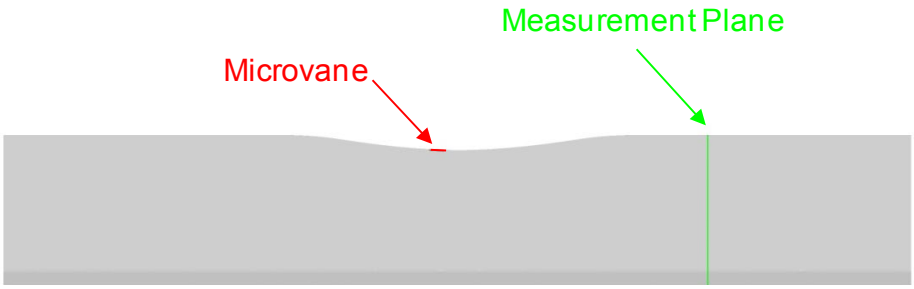

Figure 28.—Side view of computational domain with microvane (red) and data measurement plane (green).

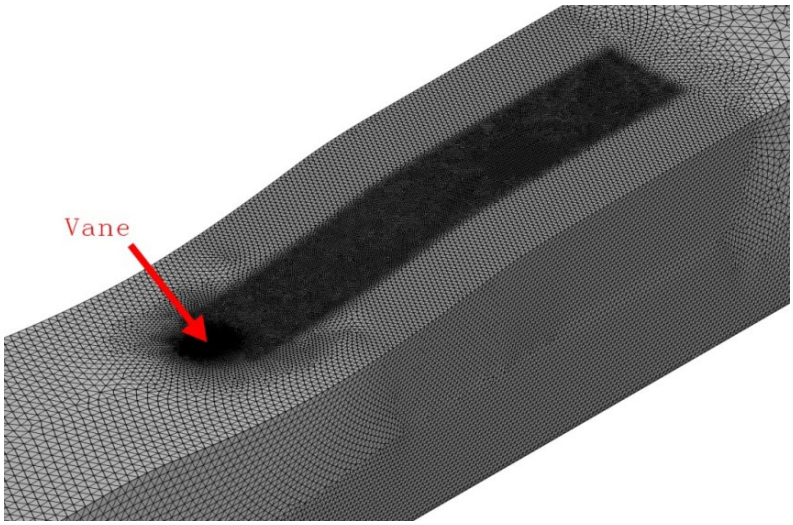

Figure 29.—Wake refinement downstream of the microvane.

Three levels of grid density were examined in the grid-convergence study. The first level of refinement produced a grid containing 5.2-million cells with an element size of 0.05 in. Refining to the second level resulted in a grid with 7.4-million cells and an element size of 0.023 in. The final refinement resulted in a 21.8-million-cell grid with an element size of 0.01 in. Normalized velocity contours are shown in Figure 30 to Figure 33 for the four grids. The black lines on the images represent the spanwise locations at which boundary layer profiles, Figure 34, were extracted. The change in the vortex shape due to grid density variation was most noticeable between the coarse, Figure 30 and level 1, Figure 31 grids. A slight sharpening of the blue upwash peak can be seen from refinement level 1 to refinement level 2, Figure 32. Finally, there was negligible difference in the vortex shape between refinement levels 2 and 3, Figure 33. From these velocity contours, it is clear that the solution is grid independent at refinement level 2. More proof of this fact is shown in Figure 34. The legend in this plot references the coarse grid as GRS1 and subsequent refinements as GRS2, GRS3, and GRS4. The distance indicator (–3-, 0-, 3-, and 5-mm) represents how far offset from the duct centerline the profile was taken. For instance, –3 mm refers to the far left black line in Figure 30 to Figure 33. As with the velocity contours, the biggest shift in the profiles occurs between GRS1 and GRS2. There is a slight change from GRS2 to GRS3, but further refinement to GRS4 shows very little change in the velocity profiles.

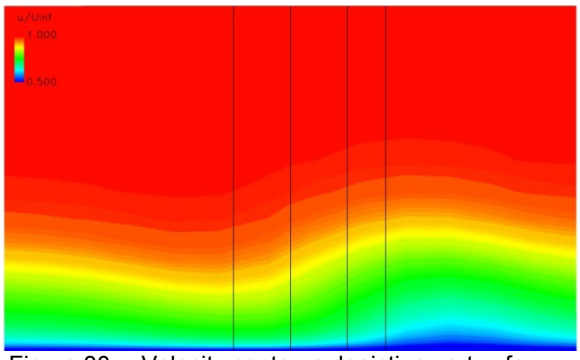

Figure 30.—Velocity contours depicting vortex for coarse grid.

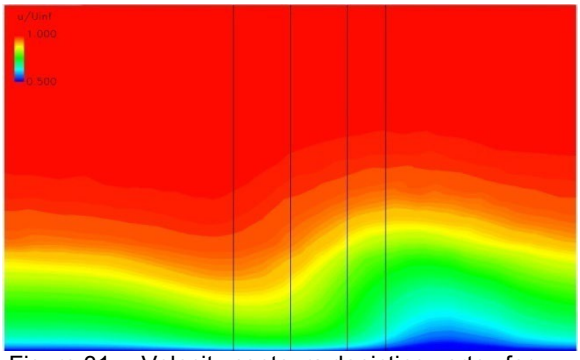

Figure 31.—Velocity contours depicting vortex for level 1 refined grid.

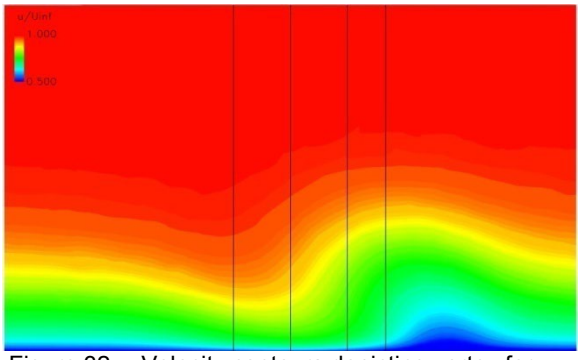

Figure 32.—Velocity contours depicting vortex for level 2 refined grid.

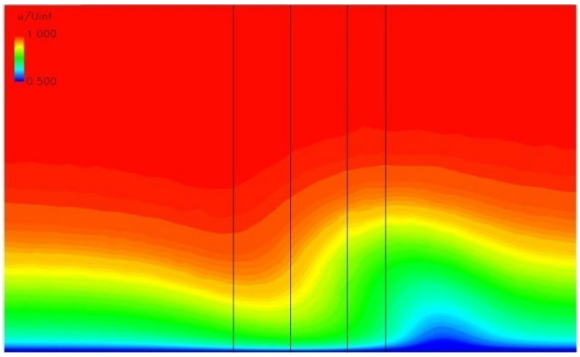

Figure 33.—Velocity contours depicting vortex for level 3 refined grid.

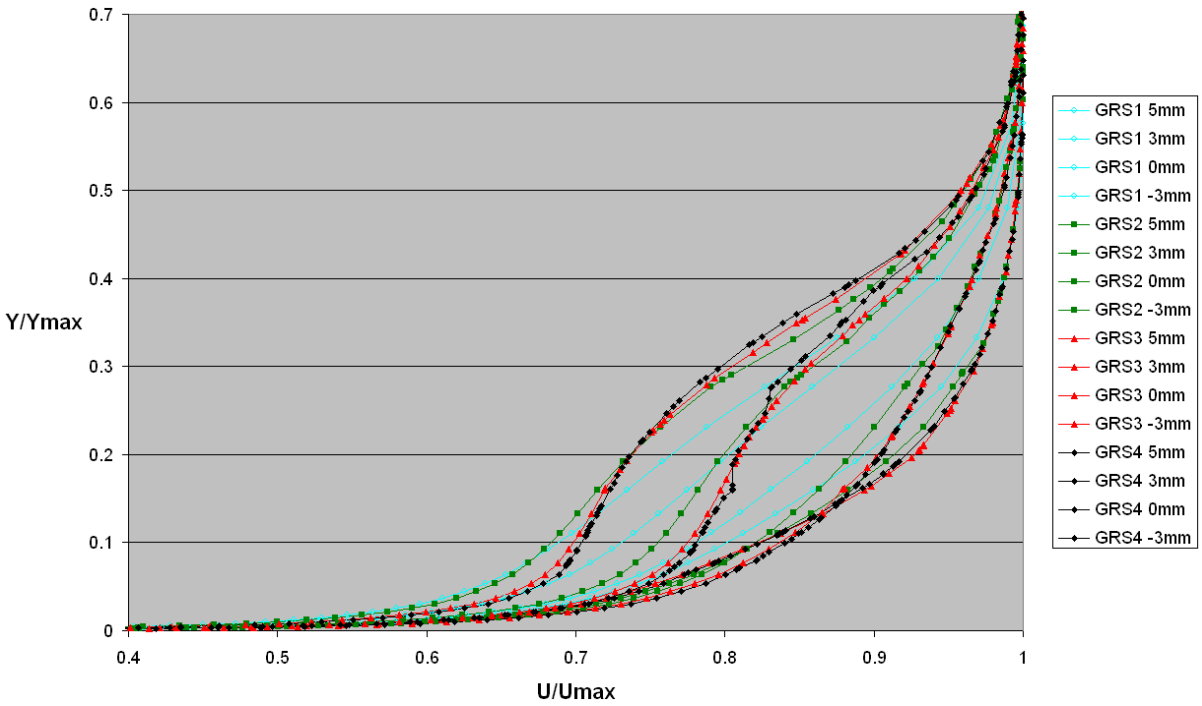

Figure 34.—Velocity profiles depicting grid convergence.

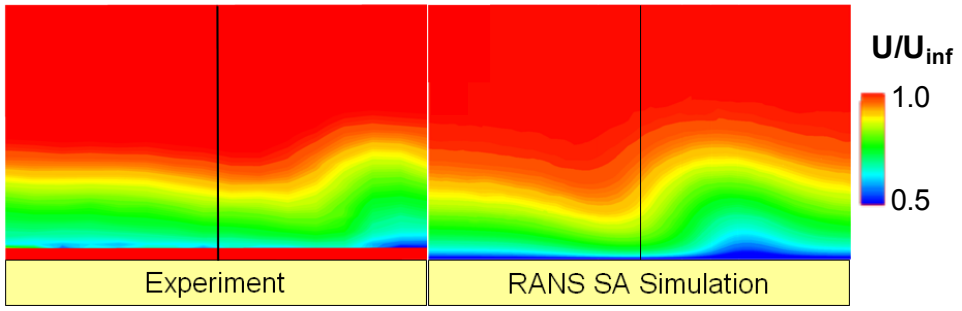

Figure 35.—Comparison of measured versus predicted vortex downstream of a microvane.

Validation of predicted against measured velocity profiles downstream of the microvane showed that the SA turbulence model with grid spacing in the microvane wake of 0.023 in. most accurately captured the microvane-induced vorticity in an adverse pressure gradient in Mach 0.5 flow. In general, the simulations over-predicted the strength of the vortex, especially the downwash component. However, the simulation captured the qualitative shape of the vortex and overall effects. Figure 35 shows velocity contours indicating that the height, width, and structure of the vortex compared well with the experiment. The black line indicates the duct centerline location. The difference between the measured and predicted spanwise vortex location, downstream of the device could be due to the fact that the predicted, CCW-rotating vortex was stronger than the measured vortex, enabling it to move farther outboard from the centerline as it propagated downstream. The overprediction of the vortex strength was attributed to the fact that the simulations did not accurately capture the corner-flow effects, which serve to dissipate the vortex strength.

Turbulence Model Sensitivity

The sensitivity of the predicted boundary-layer profiles and induced vorticity to turbulence model variations was assessed for an isolated microvane installed in the 2–D, profiled-wall tunnel. SA, SA with

rotation correction (SARC), SST, and RANS versus time-averaged RANS/LES comparisons were made with experimental results to determine which model best approximates the flow physics. Figure 36 summarizes these sensitivities through visualization of boundary layer profiles at several spanwise locations. Interpretation of the data can be simplified by looking at only the extreme upwash (far left) and extreme downwash (far right) profiles for each data set. For example, the far left (7 mm) red curve for the SST RANS/LES group can be compared to the far right (–3 mm) red curve for the same group. The band enclosed by these two extremes represents the magnitude of the upwash and downwash effects, or strength of the vortex. A thicker band would correspond to a stronger vortex, while a thinner band would correspond to a weaker vortex.

The experimental results, depicted by the solid green lines labeled "GT", illustrate that the measured vortex band is thinner and thus weaker than the simulations. The time-averaged RANS/LES simulations of both SA and SST models appear to predict very similar vortex strengths, and a stronger vortex than all other models. The next strongest vortices were predicted by the RANS SST and RANS SARC models. Both of these models produce very similar results. The weakest of the simulated vortices was predicted by the RANS SA model. This model agrees reasonably well with experiment on the upwash extreme of the vortex. On the downwash extreme, however, the RANS SA model predicted a profile, which is noticeably fuller. While differences in the predicted vortices exist between models, the differences were small and the results were relatively similar between the models.

Several possibilities exist to explain difference between the measured and predicted vortices. Assuming the experimental error is negligible and the measured vortex size, strength and location are accurate, it is likely that the corner flow effects are serving to dissipate the rotational strength of the vortex. Because the simulation fails to capture the corner flow effects, (Figure 26), it produces a stronger vortex. Regardless of the cause, the differences exist very near the wall on a very small scale, and it is currently unclear how these differences will manifest themselves at the AIP, especially with the use of flow control in the s-duct.

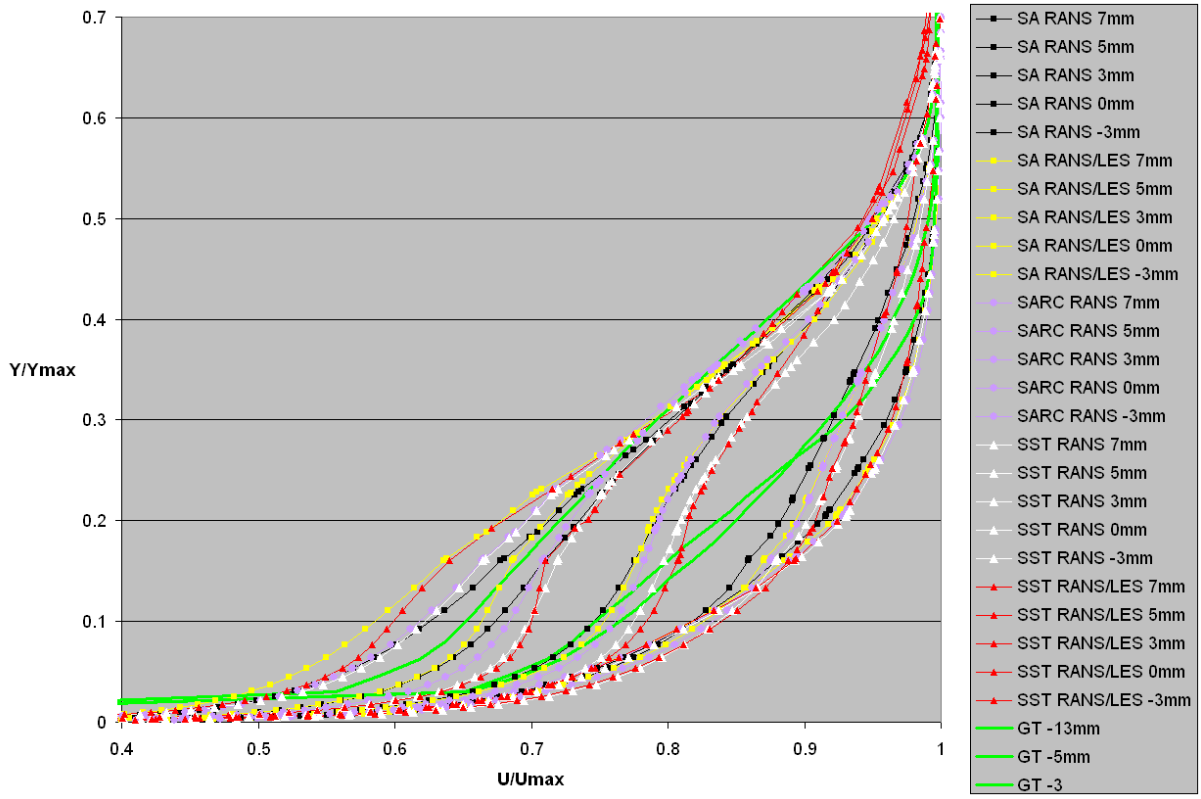

Figure 36.—Boundary layer profile sensitivity to turbulence model variations.

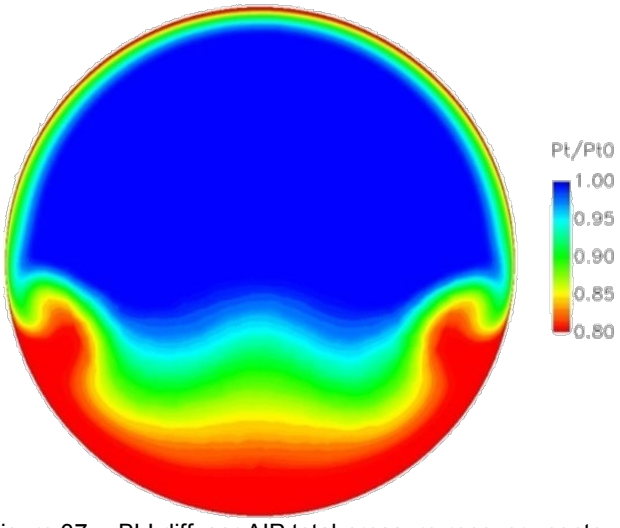

Figure 37.—BLI diffuser AIP total-pressure-recovery contours.

Numerical Simulations of a BLI Inlet Offset Diffuser

As previously stated, the application of the flow-control technologies being developed under this program will apply to a future HWB vehicle, such as the BWB. In these types of vehicles, high-speed cruise efficiency and low noise signature and fuel burn are facilitated by the use of aft-mounted, embedded engines. However, such designs pay a penalty in inlet performance and operability because the inlet ingests the large amount of low-energy, boundary-layer flow that builds up along the upper surface of the vehicle forebody. Furthermore, because the engines are embedded, the flow must pass through an s-duct, which often induces secondary flows that contribute to total pressure losses and unfavorable distortion patterns at the engine face, such as that shown in Figure 37. These patterns result in operability and fuel consumption penalties. Flow control applied in the diffuser offers the most promising solution to mitigate these challenges.

One of the objectives of this study is to provide flow-control technologies that will overcome the operability challenges of BLI inlets. Specifically, the flow control should reduce the distortion by circumferentially redistributing the low-pressure region at the bottom of the duct to create a more favorable distortion pattern at the engine face. However, the flow control must provide failsafe control of distortion without significant penalties in TSFC, supportability, or maintainability.

Numerical Simulations of BLI Offset Diffuser

Flow-control technologies for BLI inlets are being developed using an integrated, experimental and numerical approach. Initial simulations of the offset duct model in the FMRL facility were conducted to provide a preliminary assessment of the effectiveness of various flow-control approaches at improving total pressure recovery and distortion at the duct AIP. These assessments were evaluated, along with the 2–D duct experimental results, to assist in selecting the flow-control technologies most likely to meet the duct performance goals. Technologies selected through these assessments will be designed, fabricated and tested in the final year of this program. However, initial simulations of the duct test configuration, Figure 38, indicated that the test setup did not produce an accurate representation of the flow in a BLI inlet duct, Figure 39. Specifically, the AIP distortion was too low because the experimental setup did not produce the required boundary-layer thickness on the lower surface, consistent with an inlet installed on a HWB vehicle, such as the BWB. This result was anticipated and was the reason for the inclusion of provisions for the installation of a boundary-layer fence in the s-duct model.

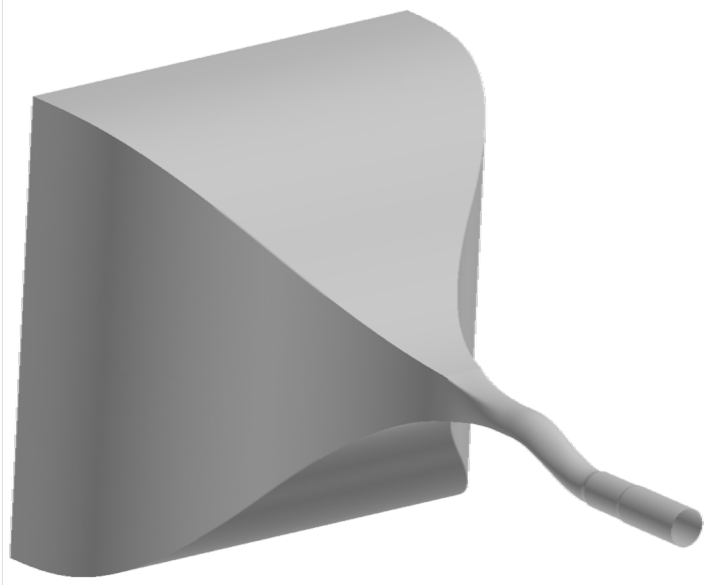

Figure 38.—Numerical model of the FMRL S-duct test configuration.

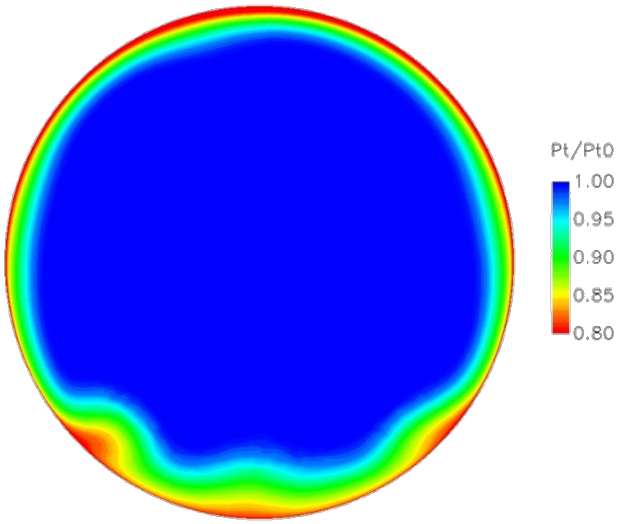

Figure 39.—AIP total-pressure contours resulting from unperturbed model inflow conditions.

Numerical methods were employed to aid in establishing the test technique required to represent BLI-inlet flow accurately in the S-duct model in the FMRL tunnel. Specifically, incoming boundary-layer profiles were imposed as boundary conditions and evaluated to determine which would result in the appropriate distortion pattern at the AIP, Figure 37. Iterations on various, simulated approach boundary conditions showed that the boundary layer shape, not the thickness, controlled the distortion pattern at the AIP. To achieve the necessary AIP recovery pattern, Figure 37, the boundary-layer profile shown in Figure 40 was imposed as a boundary condition in a structured grid, upstream of the duct, in the computational domain. This block was coupled to an unstructured-grid representation of the s-duct to complete the computational mesh. A simulation on the grid with the imposed boundary layer, Figure 40, qualitatively revealed that it would provide increased distortion at the AIP, Figure 41.

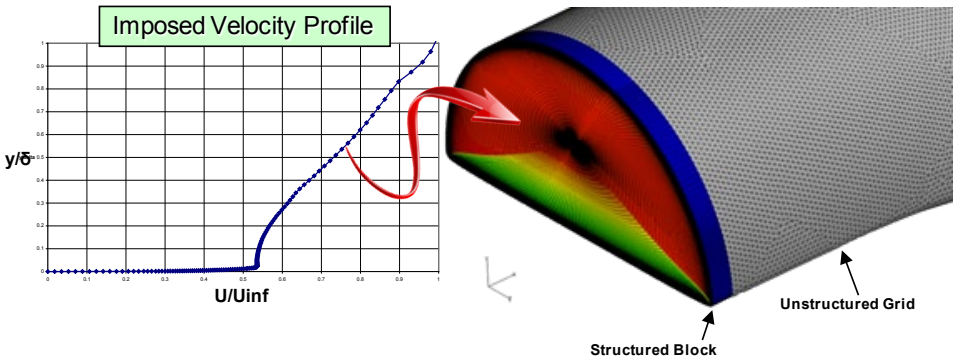

Figure 40.—BLI inlet simulation velocity profile boundary condition.

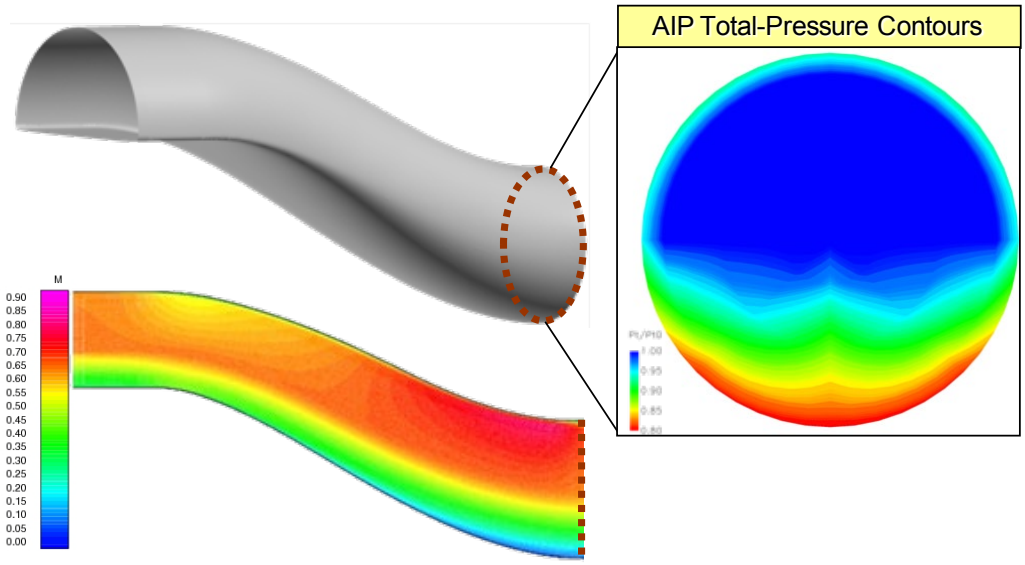

Figure 41.—Centerline Mach and AIP total-pressure contours (interpolated onto a 40-probe rake) resulting from an imposed boundary-layer flow condition.

In the absence of an imposed boundary-layer perturbation, the distortion, $DPCP_{ave}$, at the AIP was 0.015. However, by imposing a modified boundary-layer profile, the AIP distortion, $DPCP_{ave}$, increased to 0.058. This level of distortion is consistent with distortion measurements in uncontrolled BLI inlet tests (Owens, Allan, and Gorton, 2006) and provides a more realistic baseline for analyzing the effectiveness of flow-control devices. As a result, the modified boundary-layer profile was imposed as a boundary condition on the subsequent numerical simulations of the test s-duct with flow control.

Numerical Simulations of Flow Control in a BLI Offset Diffuser

RANS simulations of the s-duct configuration were generated with a number of flow-control concepts in order to provide a preliminary assessment of the effectiveness of various technologies at controlling distortion and recovery in a BLI duct. All simulations included the imposed boundary layer described in the previous section. The geometry employed for this assessment was the numerical model of the test configuration, Figure 38. All flow-control devices simulated in the s-duct were located at ~13 in. upstream of the AIP Figure 42. The flow-control devices examined numerically were all passive devices and included arrays of microramps, as well as arrays of microvanes at various heights and spacing. The initial flow-control device evaluated using RANS simulations in the s-duct was an array of microramps.

The array consisted of nine microramps evenly distributed across the lower surface of the duct. The microramp design was derived from guidelines developed at Boeing and GRC (Anderson et al. 2004, 2006). The device guidelines employed were consistent with those applied to design the passive devices tested in the 2–D wind tunnel. Actual dimensions were scaled for the duct and corresponding boundary layer. Specifically, the microramp half angle was set at 24°, and the height was defined to be 30 percent of the baseline boundary-layer height on the centerline of the duct lower surface. However, the remaining geometric parameters, namely microramp chord length and width, deviated from the guidelines. At present, guidelines do not exist specifically for BLI inlets. Applying the existing guidelines resulted in microramps that were too large for the duct. The microramp length and width was instead selected somewhat arbitrarily, using only expert opinion.

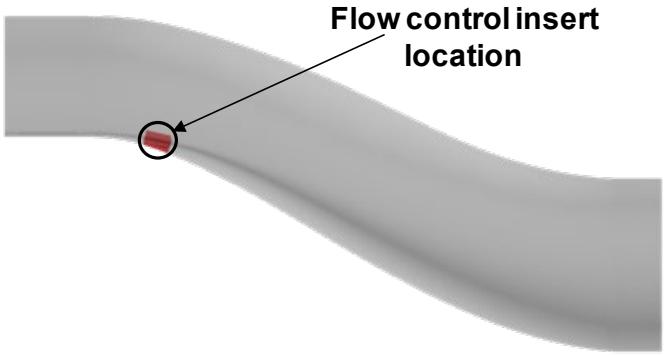

Figure 42.—Location at which flow control was simulated in the S-duct.

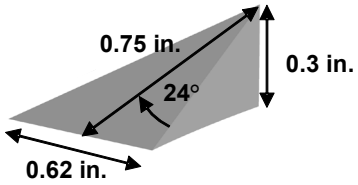

Figure 43.—Microramp flow-control device dimensions.

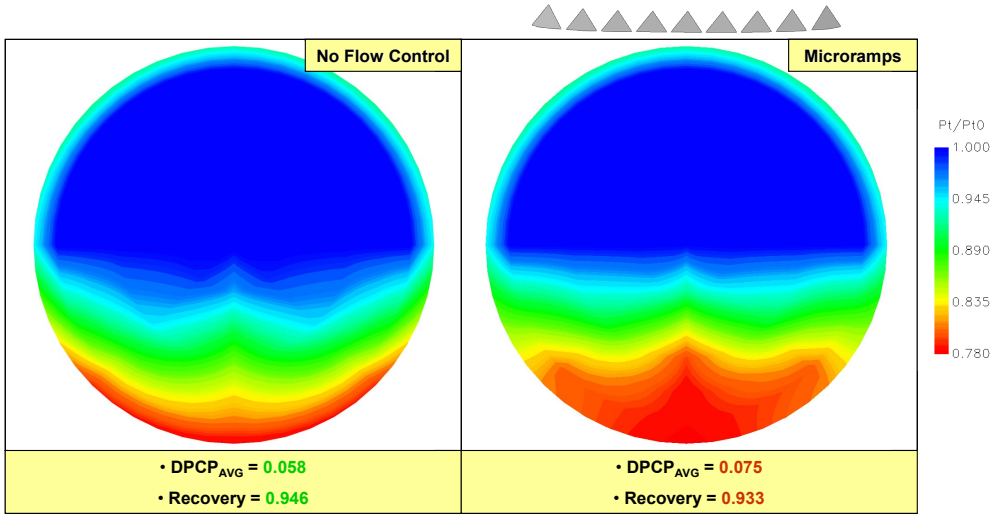

Figure 44.—AIP recovery and distortion for baseline and microramp flow control.

Results of the numerical simulations indicated that the microramps were not effective at controlling BLI inlet distortion. Specifically, the simulations showed that the microramps decrease recovery and increase distortion, Figure 44. This result was not surprising given that large-scale flow structures are required to reduce AIP distortion by redistributing the low-pressure, boundary-layer flow that pools in the lower half of the AIP in the baseline duct simulation. Microramps create small-scale structures that are useful for energizing a boundary layer and potentially preventing flow separation. However, they do not create the large-scale vortices necessary to redistribute the boundary layer of a BLI inlet at the AIP.

Unlike microramp arrays, microvane arrays have been used to create large-scale, vortical structures. For example, they have been used in diffuser applications to combat the adverse effects of secondary flow in highly offset diffusers. Several microvane configurations including straight, tapered, half-height, and a sparse array were evaluated numerically to gain a sense of the design factors to which BLI inlet performance would be sensitive. The microvane geometries, Figure 45, employed in the numerical simulations were derived from optimized BLI inlet microvane geometries (Allan, Owens, and Lin, 2006). Tapered and rectangular cross-section microvane geometries were simulated. In addition, half-height microvanes, which were identical to the tapered microvanes but with the top half removed, were also simulated. Finally, a sparse array, which was identical to the tapered array but with the four center microvanes removed was also analyzed.

A comparison of the baseline simulation to that of the straight microvane array, Figure 46, shows that the distortion, $DPCP_{ave}$, dropped from 0.058 to 0.014 with the use of the straight microvane array, while the recovery experienced a 1.7 percent decrease. The microvanes produce individual vortices that coalesce into two, large-scale, counter-rotating vortices as they propagate downstream in the duct. These large-scale structures redistribute the single, low-pressure region in the lower half of the duct such that the resulting distortion pattern is one that will be more favorable in terms of engine operability.

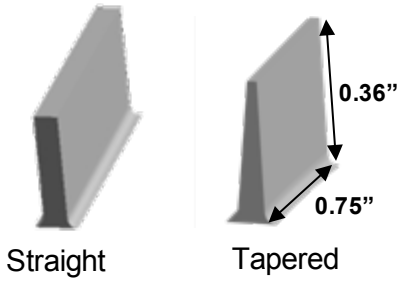

Figure 45.—Geometry and dimensions of the straight and tapered microvanes.

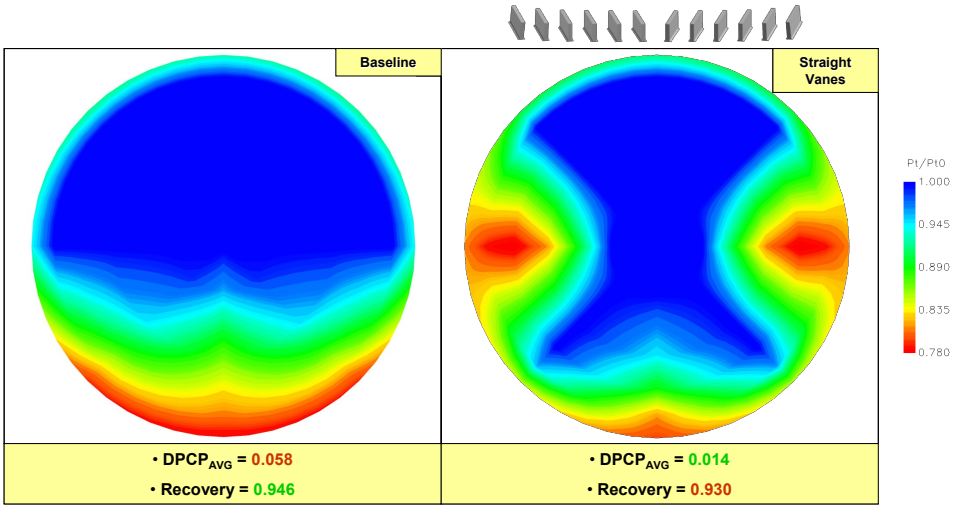

Figure 46.—Baseline distortion and recovery compared to a straight microvane array.

A comparison of simulated total-pressure contours at the AIP of the duct with a tapered microvane-array with those at the AIP of a duct with straight microvane-array flow control indicates that the tapered microvanes decrease distortion, $DPCP_{ave}$, from 0.058 to 0.013 and increase recovery by 0.32 percent, Figure 47. Strictly from an inlet performance standpoint, the tapered microvanes perform better than straight microvanes. However, it is possible that they will fall short on reliability and/or supportability. Nevertheless, both the tapered and straight microvane arrays appear to provide significant distortion improvements with only moderate recovery penalties in BLI inlet ducts. In the absence of a system-level assessment of tapered versus straight microvane arrays, tapered microvanes were selected as the microvane shape with which to move forward based solely on the predicted inlet performance benefits.

In addition to the microvane cross-section shape, height and spacing parametrics were also examined numerically. A comparison between the tapered microvane array, a half-height microvane array, and a sparse microvane array shows that all the configurations have comparable recovery. Distortion, however, is significantly higher in the case of the half-height microvanes, but only slightly higher with the sparse array, Figure 48. This suggests that the flow could be sufficiently controlled by using fewer microvanes, or even by using the half-height microvanes in conjunction with synthetic jets. Results from these initial microvane parametrics substantiated the need for a more structured, systematic assessment of the sensitivity of inlet performance to microvane geometric factors.

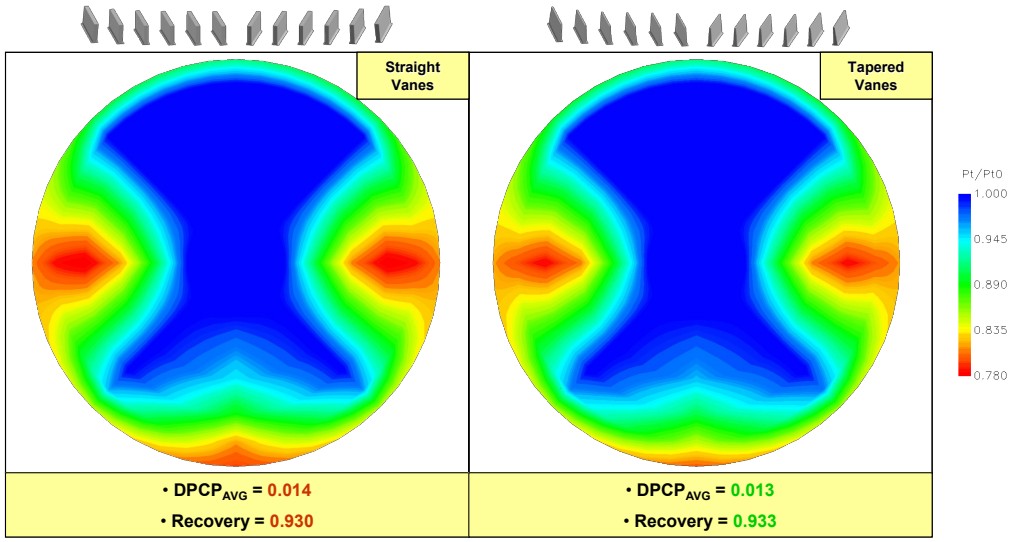

Figure 47.—Straight microvane recovery and distortion compared to a tapered microvane array.

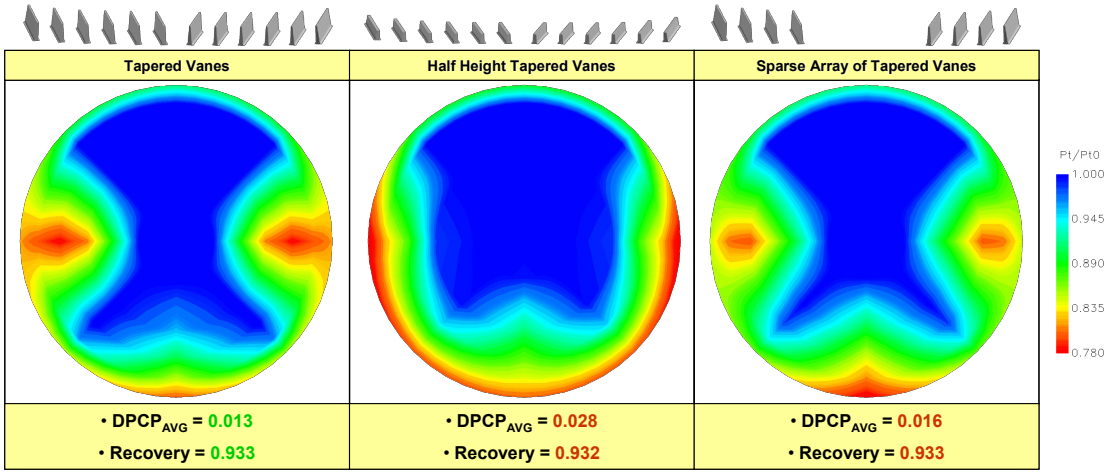

Figure 48.—Comparison of recovery and distortion between three microvane configurations.

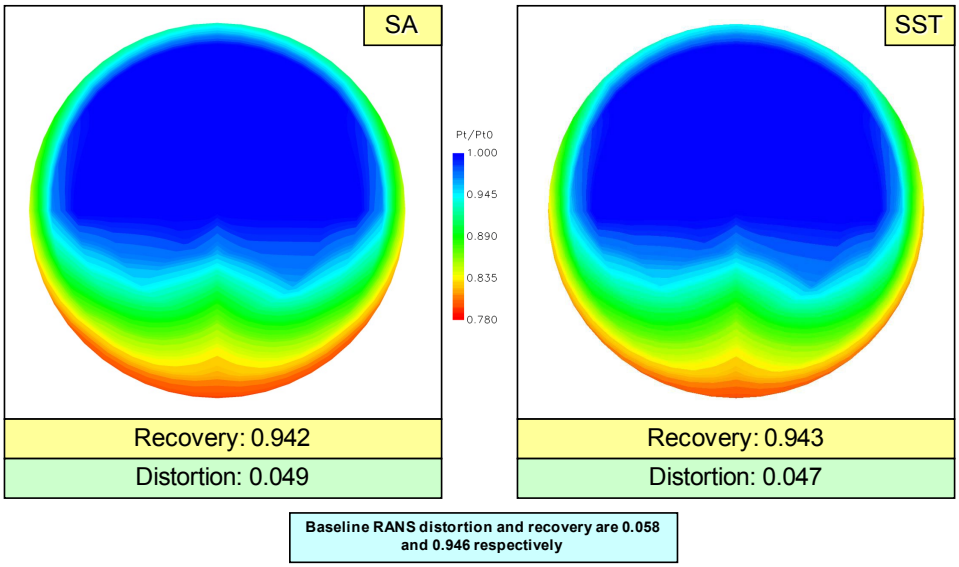

Figure 49.—Dynamic distortion simulations with SA and SST turbulence models.

Dynamic Distortion Simulations

In support of the program objective to improve flow-control prediction tools, time-dependent, numerical simulations have been made of the baseline s-duct in an effort to determine how to model dynamic distortion accurately. Both SA and SST turbulence models have been employed with a hybrid RANS/LES model to capture the time-dependent effects in the s-duct. The time step of the simulations was 0.09 ms, with one solution being recorded every 10-time steps (0.9 ms). The results shown in Figure 49 are AIP recovery contours averaged over 110 saved solutions (~99 ms). The first solution in the average is taken after the flow has convected through the duct ~3 times (~110 ms), and the final solution is the average ~99 ms after that.

The two solutions exhibit minute differences from one another. When compared with the RANS simulation, the recovery decreases almost insignificantly, while the distortion realizes a drop of ~17 percent. The similarity of recovery and drop in circumferential distortion, $DPCP_{ave}$, between steady state and time-dependent simulations has been observed in other BLI S-duct simulations conducted previously in Phase 1 of this program.

Conclusions

The Boeing IFCPT program is developing enabling technologies and validated prediction tools for controlling inlet total-pressure distortion that will be applicable across a broad range of future aircraft, including subsonic, HWB vehicles. Specifically, fail-safe, hybrid flow-control technologies consisting of closely coupled microvanes and synthetic jets are being designed and evaluated as a means to control BLI-inlet distortion. In addition, advanced, inlet-distortion prediction methods based on integrated CFD and testing, using statistically designed experiments are being developed and validated.

The flow-control strategy aimed at counteracting AIP distortion resulting from significant inlet-boundary-layer ingestion is to redistribute the concentrated, low total pressure, boundary-layer flow more evenly around the perimeter of the AIP, thus creating a distortion pattern to which engines are typically more tolerant. This result may be achieved by using flow control to generate two, large-scale, counter-rotating vortices that sweep the concentrated boundary layer flow up and around the outer perimeter of the AIP. To accomplish this, an array of streamwise vortices must be generated such that they merge into a large-scale vortex farther downstream in the duct, which requires consideration of the vortex sources, sizes and spacing. It is this prerequisite that dictates the packing density and number of devices. The use of a hybrid system, in place of a

passive system offers the potential of reducing the required number of microvanes, thereby potentially reducing total-pressure losses, maintainability, and supportability challenges.

Experimental results obtained during the current reporting period were based on a 2–D, profiled wall test section in which detailed flow measurements were obtained in the vicinity of individual or at most, a device pair. During year three of the current program, the results of the isolated-device tests will be used to guide the selection of and aid in understanding the physics associated with flow-control actuation in an offset, BLI inlet S-duct. During the current reporting period, detailed model design and fabrication of the offset duct test hardware was completed. Model installation in the Georgia Institute of Technology FMRL and testing of this hardware is planned to commence in early FY10.

During the current reporting period, the interaction of surface-mounted passive and active flow-control devices with a Mach 0.5 cross flow was examined in a small-scale wind tunnel. The evolution of streamwise vortices induced by the flow control was investigated in an adverse pressure gradient that mimics the pressure gradient within a diffuser compatible with future HWB vehicles. Counter-rotating vortex pairs and single-sense vortices were formed and characterized using passive microramps and microvanes, respectively. Similar streamwise vortices were also generated using synthetic jet actuators. The jets had rectangular orifices that were either slanted and/or skewed to produce single-sense vortices or streamwise aligned to produce vortex pairs. Finally, hybrid actuation approaches were demonstrated where a passive microvane and active synthetic jet were designed and operated in a tandem arrangement such that the induced vorticity from the active device enhanced the effects of the passive device, improving the overall control effectiveness.

During the current reporting period, integration of a synthetic jet with a pair of microvanes was proven to enhance the weakly interactive vortices resulting from passive microvane actuation. Specifically, hybrid synthetic jet/microvane flow control resulted in vortices that merged into one large, coherent structure. Implementation of a row of synthetic jets followed by a row of microvanes could be made more efficient by implementing this concept of merging vortices. Furthermore, hybrid microvane/jet devices offer the benefit of reducing distortion with a reduced size or number of microvanes, thus offering potential improvements in recovery, as well as, system-level requirements such as supportability and maintainability.

Experimental data from the flow-control-device characterization studies were also used to validate numerical prediction tools. Numerical simulations were carried out using the 3–D, viscous, Navier-Stokes CFD code, BCFD. The baseline wind tunnel, in the absence of flow control was simulated, as was the wind tunnel with a single microvane. The RANS turbulence models produced similar results for the baseline tunnel, but failed to accurately predict the corner flows of the 2–D test section. The inaccurately modeled corner flow was assumed to be the result of inadequate grid density in that region. A grid-resolution study was conducted on the microvane geometry in the 2–D test section. Four levels of grid density were considered. Grid independence was established with the second refinement, which determined the necessary element size for future simulations of the microvane. Numerical results based on SA, SARC, SST turbulence models, as well as RANS and time-averaged RANS/LES solutions were compared with experimental data downstream of a microvane. All the numerical schemes yielded similar results and overpredicted the strength of the induced vorticity of a microvane. The SA model produced the closest approximation to the measured vortex strength.

Numerical simulations of a Boundary-Layer-Ingesting (BLI) offset inlet duct consistent with that in the BWB vehicle were conducted during the current reporting period. These simulations were used to support the development of the test technique for simulating BLI inlet flow in an isolated diffuser. Specifically, a boundary-layer profile that could be replicated experimentally with a fence, was applied at the duct entrance to generate the thick boundary layer consistent with BLI inlets.

In addition to the test technique, microvane and microramp, passive, flow-control devices were simulated in the offset BLI inlet duct to compare the predicted performance benefits of these devices at the aerodynamic interface plane (AIP). The flow-control devices examined numerically were all passive devices and included arrays of microramps, as well as arrays of microvanes at various heights and spacing. Benefits were quantified in terms of recovery improvement and distortion reduction from the

baseline, non-actuated flow. Microvane arrays were found to be significantly more effective than microramp arrays at improving recovery and distortion in BLI inlet ducts, as they produced the large-scale vortical structures necessary to redistribute the ingested, low-energy boundary layer fluid into more favorable engine-face pattern. Results from the initial microvane parametrics showed significant inlet-performance sensitivity to changes in microvane geometric factors, indicating that significant performance gains with reduced supportability and maintainability penalties could be realized through optimizing the devices and pairing them with active components.

Finally, Spalart-Allmaras and SST turbulence models have been employed with a hybrid RANS/LES model to simulate the time-dependent effects and attempt to predict dynamic distortion accurately in an offset, BLI inlet duct. This work will continue into the final year of this program. As experimental data is obtained for the duct test configurations, numerical simulations will be validated against the data. Using this data, the prediction tool will be enhanced to predict dynamic distortion more accurately in offset diffusers.

Future Work

In the final year of Phase 2, detailed experimental testing of active, hybrid flow-control devices and numerical prediction tool development will continue. BLI-inlet-duct simulation testing will commence and ultimately be used to generate a database of steady-state performance sensitivities to flow-control devices and design parameters. Specifically, flow control design guidelines will be generated, and the most promising technologies will be identified. The benefits of flow control in BLI inlet ducts will be quantified in terms of steady state and dynamic total-pressure recovery and distortion. The dynamic data will provide the basis for validation of a new numerical dynamic distortion simulation tool.

In addition to the experimental investigations in an offset BLI inlet duct, numerical simulations of the test geometry with and without flow control will continue in the final year of this effort. Unsteady, Navier-Stokes codes with a hybrid RANS/LES turbulence model will be employed to predict dynamic distortion in the BLI inlet duct. Predicted results will be compared with experimental data. Results of these comparisons will be used to improve the distortion-prediction tool and make it available for incorporation into the Wind-US NPARC Alliance code.

Lastly, system-level payoffs and penalties will be assessed for flow-control technologies in an offset, BLI inlet diffuser. This assessment will include conceptual layouts of diffusers integrated in HWB aircraft and tailored with flow-control systems, Figure 50. System-level impacts will be assessed based on existing sensitivities in terms of TOGW, performance (TSFC), and risk.

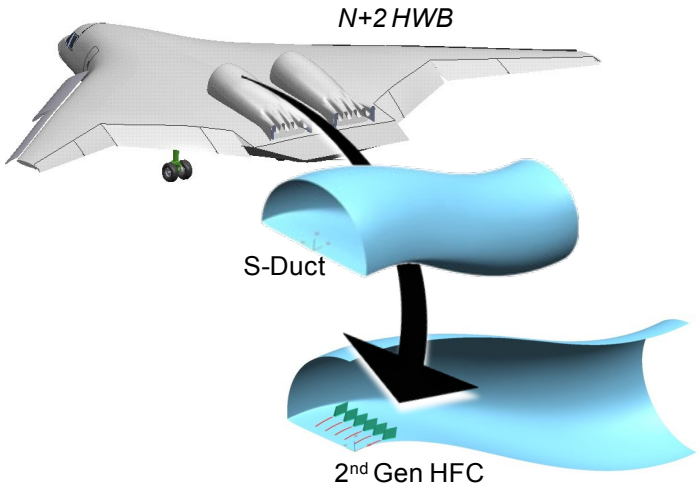

Figure 50.—BLI inlet offset diffuser with flow control.

Appendix.—Nomenclature

AIP	aerodynamic interface plane
AFLR	Advancing-Front/Local-Reconnection
BCFD	Boeing Computational Fluid Dynamics
BLI	boundary layer ingesting
BWB	blended wing body
CCW	counter-clockwise
CD	converging-diverging
CFD	Computational Fluid Dynamics
CRSV	counter-rotating streamwise vortices
CW	clockwise
$DPCP_{ave}$	SAE average circumferential total pressure distortion descriptor
δ	boundary layer thickness
δ_{apex}	boundary-layer thickness at the wind-tunnel-test-section apex
FMRL	Fluid Mechanics Research Laboratory
GaTech	Georgia Institute of Technology
GRC	NASA Glenn Research Center
h	shape factor
h_0	baseline shape factor
HFC	hybrid flow control
HLLE	Harten-Lax-van Leer-Einfeldt
HWB	Hybrid Wing Body
IFCPT	inlet flow control and prediction technologies
LES	Large Eddy Simulation
M	Mach number
MADCAP	Modular Aerodynamic Design Computational Analysis Process
P_0	ambient pressure
PIV	particle image velocimetry
P_T	total pressure
RANS	Reynolds Averaged Navier-Stokes
RSM	response surface model
SA	Spalart-Allmaras
SST	shear-stress-transport
SARC	Spalart-Allmaras with rotation correction

TRL	Technology Readiness Level
T_T	total temperature
U	streamwise velocity
U*	time-averaged streamwise velocity
ΔU	streamwise velocity difference relative to the baseline
V	cross-stream velocity
V*	time-averaged cross-stream velocity
x	streamwise direction
y	vertical direction
z	spanwise direction

References

Allan, B, Owens, L, and Lin, J. (2006), "Optimal Design of Passive Flow Control for a Boundary-Layer-Ingesting Offset Inlet Using Design-of-Experiments," AIAA–2006–1049.

Amitay, M., Pitt, D., and Glezer, A. (2002), "Separation Control in Duct Flows," Journal of Aircraft, 39, 616–620.

Amitay, M., Smith, B., and Glezer, A. (1998), "Aerodynamic flow control using synthetic jet technology,"AIAA–98–0208.

Anabtawi, A.J., Blackwelder, R.F., Lissaman, B.S.P, Liebeck, R.H. (1999), "An Experimental Investigation of Boundary Layer Ingestion in a Diffusing S-Duct With and Without Passive Flow Control," AIAA–99–0739.

Anderson, B.H., Mace, J.L., Mani, M. (2009), "Active "Fail Safe" Micro-Array Flow Control For Advanced Embedded Propulsion Systems," AIAA–2009–741.

Anderson, B.H., Miller, D.N., Addington, G.A., Agrell, J. (2004), "Optimal Micro-Jet Flow Control for Compact Air Vehicle Inlets," NASA/TM—2004-212937.

Anderson, B., Tinapple, J., and Surber, L. (2006), "Optimal Control of Shock Wave Turbulent Boundary Layer Interactions Using Micro-Array Actuation,"AIAA–2006–3197b.

Anderson, B., Tinapple, J., and Surber, L. (2006, Jun.), "Optimal Control of Shock Wave Turbulent Boundary Layer Interactions Using Micro-Array Actuation," San Francisco, CA: AIAA–2006–3197.

Compton, D.A. and Johnston, J.P. (1992), "Streamwise vortex production by pitched and skewed jets in a turbulent boundary layer," AIAA J., 30, 640–647.

Kim, W., and Menon, S. (1999), "An Unsteady Incompressible Navier-Stokes Solver for Large Eddy Simulation of Turbulent Flows," International Journal for Numerical Methods in Fluids, 31, 983–1017.

Lin, J.C. (2002), "Review of research on low-profile vortex generators to control boundary-layer separation," Progress in Aerospace Sciences, 38, 389–420.

Mani, M. (2004, Jan.-Feb.), "Hybrid Turbulence Models for Unsteady Flow Simulations," Journal of Aircraft , 41 (1).

Mani, M., Cary, A., and Ramakrishnan, S. (2005, Jul.-Aug.), "A General Purpose Euler and Navier-Stokes Solver for Structured and Unstructured Grids," AIAA J. of Aircraft, Vol. 42, No.4, pp. 991–997.

Mani, M., Winkler, C., Fisher, M., and Mackie, S. (2007), "A post Processing Approach for CFD Error Associated with Grid Resolution," 45th AIAA Aerospace Sciences Meeting, Reno, NV, AIAA–2007–66809.

Menter, F. (1993), "Zonal Two Equation k-Turbulence Models for Aerodynamic Flows," 24th Fluid Dynamics Conference, Orlando, FL, AIAA–93–2906.

Owens, L., Allan, B., and Gorton, S. (2006), "Boundary-Layer-Ingesting Inlet Flow Control," AIAA–2006–839.

Peake, D.J., Henry, F.S., and Pearcey, H.H. (1999), "Viscous Flow Control with Air-Jet Vortex Generators," AIAA Paper 1999–3175.

Shin, A., Vanka, S., Mani, M., Dorgan, A., and Michal, T. (2007), "Application of BCFD unstructured Grid to Simulation of Microramp Control of Shock/Boundary Layer Interaction," AIAA CFD Conference, Miami, FL.

Smith, B., and Glezer, A. (1998), "The Formation and Evolution of Synthetic Jets," Physics of Fluids, 10 (9).

REPORT DOCUMENTATION PAGE	Form Approved OMB No. 0704-0188

1. REPORT DATE *(DD-MM-YYYY)*	2. REPORT TYPE	3. DATES COVERED *(From - To)*
01-10-2010	Final Contractor Report	

4. TITLE AND SUBTITLE
Inlet Flow Control and Prediction Technologies for Embedded Propulsion Systems
Summary Report for Fiscal Year 2009

5a. CONTRACT NUMBER
NNC07CB76C

5b. GRANT NUMBER

5c. PROGRAM ELEMENT NUMBER

6. AUTHOR(S)
McMillan, Michelle, L.; Gissen, Abe; Vukasinovic, Bojan; Lakebrink, Matthew, T.; Glezer, Ari; Mani, Mori; Mace, James

5d. PROJECT NUMBER

5e. TASK NUMBER

5f. WORK UNIT NUMBER
WBS 561581.02.08.03.21.66

7. PERFORMING ORGANIZATION NAME(S) AND ADDRESS(ES)
The Boeing Company
P.O. Box 516
MS 064 1231
St. Louis, MO 63134

8. PERFORMING ORGANIZATION REPORT NUMBER
E-17405

9. SPONSORING/MONITORING AGENCY NAME(S) AND ADDRESS(ES)
National Aeronautics and Space Administration
Washington, DC 20546-0001

10. SPONSORING/MONITOR'S ACRONYM(S)
NASA

11. SPONSORING/MONITORING REPORT NUMBER
NASA/CR-2010-216779

12. DISTRIBUTION/AVAILABILITY STATEMENT
Unclassified-Unlimited
Subject Categories: 02, 07, and 34
Available electronically at http://gltrs.grc.nasa.gov
This publication is available from the NASA Center for AeroSpace Information, 443-757-5802

13. SUPPLEMENTARY NOTES

14. ABSTRACT
Fail-safe inlet flow control may enable high-speed cruise efficiency, low noise signature, and reduced fuel-burn goals for hybrid wing-body aircraft. The objectives of this program are to develop flow control and prediction methodologies for boundary-layer ingesting (BLI) inlets used in these aircraft. This report covers the second of a three year program. The approach integrates experiments and numerical simulations. Both passive and active flow-control devices were tested in a small-scale wind tunnel. Hybrid actuation approaches, combining a passive microvane and active synthetic jet, were tested in various geometric arrangements. Detailed flow measurements were taken to provide insight into the flow physics. Results of the numerical simulations were correlated against experimental data. The sensitivity of results to grid resolution and turbulence models was examined. Aerodynamic benefits from microvanes and microramps were assessed when installed in an offset BLI inlet. Benefits were quantified in terms of recovery and distortion changes. Microvanes were more effective than microramps at improving recovery and distortion.

15. SUBJECT TERMS
Aerodynamics; Boundary layer control; Turbulent boundary layer; Jet control; Vortex generators; Computational fluid dynamics; Turbulence models

16. SECURITY CLASSIFICATION OF:			17. LIMITATION OF ABSTRACT	18. NUMBER OF PAGES	19a. NAME OF RESPONSIBLE PERSON
a. REPORT	b. ABSTRACT	c. THIS PAGE			STI Help Desk (email:help@sti.nasa.gov)
U	U	U	UU	48	19b. TELEPHONE NUMBER *(include area code)* 443-757-5802